# EXPERIMENTTAL CONDITIONS TO TEST EXTERNAL FIELD EFFECT IN MODIFIED NEWTONIAN DYNAMICS

# **PENG CHENGXIAOHE**

XIAMEN UNIVERSITY MALAYSIA 2025



#### FINAL YEAR PROJECT REPORT

# EXPERIMENTAL CONDITIONS TO TEST EXTERNAL FIELD EFFECT IN MODIFIED NEWTONIAN DYNAMICS

NAME OF STUDENT : PENG CHENGXIAOHE

STUDENT ID : PHY2109518

SCHOOL/ FACULTY : SCHOOL OF MATHEMATICS AND PHYSICS

PROGRAMME : BACHELOR OF SCIENCE IN PHYSICS

(HONOURS)

INTAKE : 2021/09

SUPERVISOR : PROF. Tomasz Paterek

CO-SUPERVISOR : ASSOC PROF. Lim Yen Kheng

#### **DECLARATION**

I hereby declare that this project report/ thesis is based on my original work except for citations and quotations which have been duly acknowledged. I also declare that it has not been previously and concurrently submitted for any other degree or award at Xiamen University Malaysia or other institutions.

Name : Peng Chengxiaohe

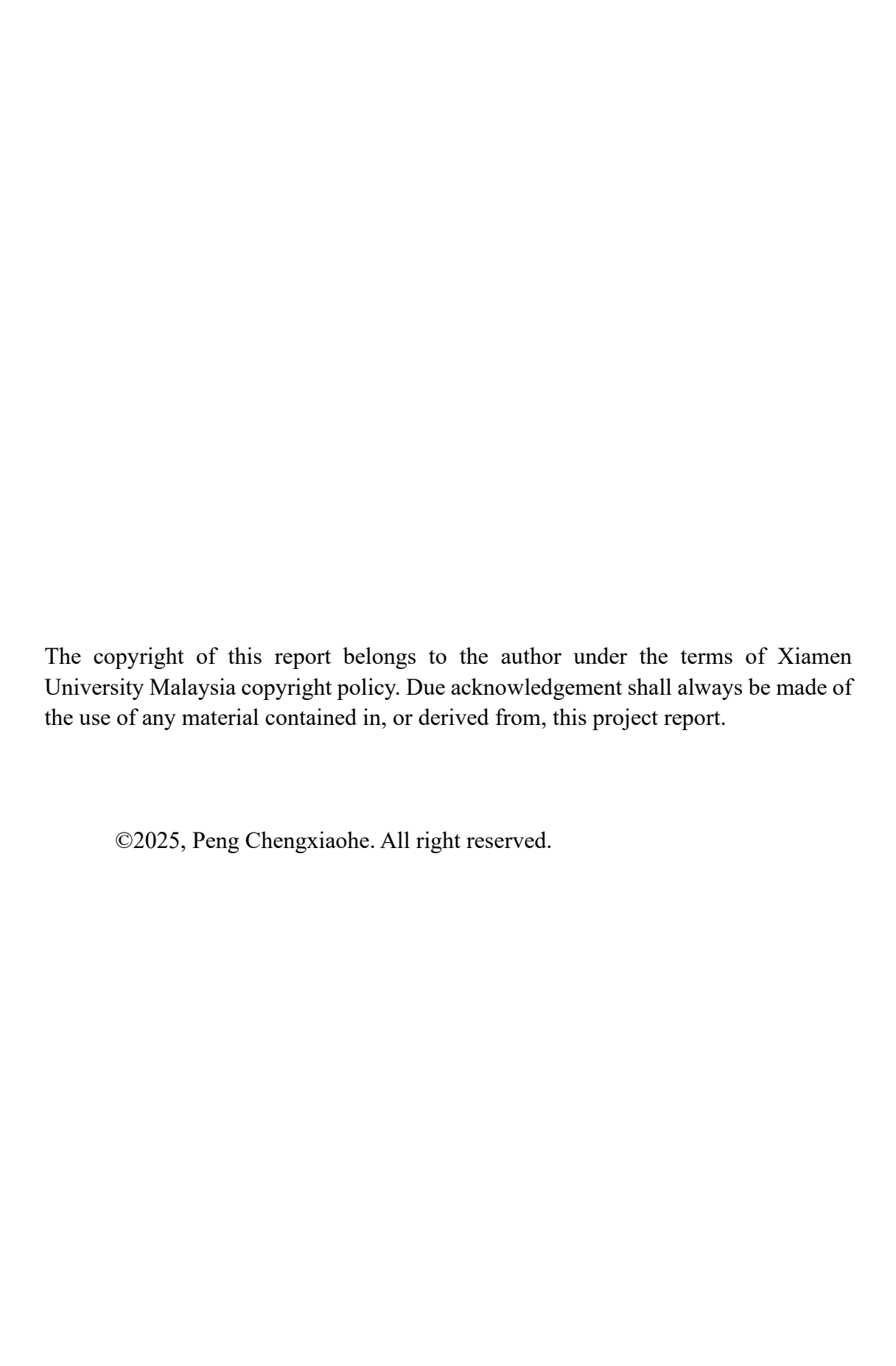
ID No. : PHY2109518

Date :2025/6/25

#### APPROVAL FOR SUBMISSION

I certify that this project report/ thesis entitled "EXPERIMENTTAL CONDITIONS TO TEST EXTERNAL FIELD EFFECT IN MODIFIED NEWTONIAN DYNAMICS" was prepared by PENG CHENGXIAOHE has met the required standard for submission in partial fulfillment of the requirements for the award of Bachelor of PHYSICS at Xiamen University Malaysia.

Approved by,	
	· Tomasz Pateret
Signature	: Tomasz Jakonet
Supervisor	: Prof. Tomasz Paterek
Date	: <u>25 June 2025</u>
Signature	<u>du</u>
Co-Supervisor	: Assoc. Prof Lim Yen Kheng
Date	: 26/06/2025



#### **ACKNOWLEDGEMENTS**

I wish to thank all the teachers, classmates and family members who have helped me with this thesis.

First and foremost, I am deeply grateful to my supervisors, Prof. Tomasz Paterek and Prof. Lim Yen Kheng, for their rigorous attitude and patient mentorship, which have been invaluable to my research. I also extend my thanks to all the faculty members of the School of Physics for their profound knowledge and dedicated teaching, which laid a solid foundation for my academic studies.

In addition, I want to recognize Kelvin Tang and Zhou Ziyang for their encouragement and useful suggestions throughout data collection and the writing process.

Lastly, my heartfelt appreciation goes to my family for their unwavering understanding and support, which have been my greatest motivation.

Even as I finish my college life as a undergraduate student, the close relationships and knowledge from university will never be forgotten. In the future, I will keep working hard and improving myself.

#### **ABSTRACT**

The Modified Newtonian Dynamics (MOND) offers an alternative to dark matter hypothesis by proposing a deviation from Newtonian gravity at low accelerations. An important prediction of MOND is the External Field Effect (EFE), wherein a system's internal dynamics are influenced by external gravitational fields, even if these fields are uniform. This project investigates the experimental feasibility of detecting the EFE under controlled laboratory conditions. Theoretical constraints are derived based on MOND's critical acceleration scale, ensuring that experimental setups remain within the MOND regime. A two-body system is modeled and analyzed, accounting for internal gravitational attraction, air resistance. Both analytical and numerical methods, including Runge-Kutta simulations, are employed to estimate collision dynamics under different configurations. In the external field, results show that EFE can be verified with time measurement of precision. Limitations arising from Earth's rotation and practical measurement constraints were also considered. This study provides foundational insights into designing precision laboratory tests for alternative gravity theories.

Keywords: Dark Matter, Modified Newtonian Dynamics (MOND), External Field Effect (EFE)

## TABLE OF CONTENTS

<b>DECL</b> A	ARATION	i
<b>APPRO</b>	OVAL FOR SUBMISSION	ii
ACKNO	OWLEDGEMENTS	iv
<b>ABSTR</b>	<u> </u>	V
<b>TABLE</b>	OF CONTENTS	vi
LIST O	F FIGURES	vii
LIST O	F TABLES.	ix
LIST O	F SYMBOLS	X
CHAPT	ΓER	
1	Introduction.	1
2	Dark Matter Phenomenon	
	2.1 Galactic Rotation Curve	
	2.2 Galaxy Cluster	∠
3	Theory of MOND	
	3.1 <u>Key Hypotheses of MOND</u>	
	3.2 Modified Newton's Second Law	
	3.3 Modified Gravity	
	3.4 <u>Interpolation Functions</u>	
	3.5 The External Field Effect—EFE	14
	3.6 Successes of MOND	
	2.6.1 Galaxy Rotation Curve	
	2.6.2 <u>Tully-Fisher Relation</u>	18
4	Proposed experiment	
	4.1 <u>Internal Gravity</u>	
	4.2 <u>Air Friction</u>	
	4.3 Experimental Conditions	26
	4.4 Rotating Polar Coordinate System	
	4.5 Rough Trajectory and Collision Time	
REFER	RENCES	37
APPEN	IDICES	41

## LIST OF FIGURES

Rotation curve of spiral galaxy Messier 33 [8]. The data points of color yellow

and blue with error bars is the observational data of stars' speed with respect to the distance from the center of galaxy. The gray dashed line is the theoretically expected rotation curve based solely on the distribution of visible matter. The solid line represents the best fit model of observation data. The x-axis is the radial distance from the galactic center. The origin of x-axis stands for the center of the galaxy
2.2 X-ray emission and gravitational lensing map of the Bullet Cluster 1E 0657-558. The green contours in top and bottom graphs are the gravitational lensing results. The plus symbol in the pannel on top indicates the centers of masses of plasm clouds. White bars represent distance of 200kpc
3.1 Comparison of different $\mu$ -function profiles as a function of x—the ratio of acceleration to the characteristic acceleration scale $a_0$ . The solid line and dashed line are the plots of Equation (3.4.11), with $n=1$ (simple $\mu$ -function) and $n=2$ (standard $\mu$ -function), respectively. Dotted line and dashed-dotted line are curves of Equation (3.4.13) for $m=0.5$ and $m=1$ respectively. The circular marker line and starred marker line depicts Equation (3.4.14) with $n=4$ and $n=6$ respectively (figure from [16])
3.2 MOND rotation curve fits for representative galaxies from the THINGS survey [22]. The baryonic mass of selected galaxies varies from $3 \times 10^8 M_{\odot}$ to $3 \times 10^{11} M_{\odot}$ . High-resolution interferometric 21 cm observations are available for the gaseous components of all galaxies, along with 3.6-micron photometric data to map their stellar distributions. Black line is calculated from Newtonian baryonic mass model. Blue is fit curve of MOND. The interpolating function used in the fitting curve is Equation (3.4.14) with $n=1$
3.3 The baryonic Tully-Fisher (BTF) relation is analyzed under varying stellar mass-to-light ratio assumptions, with each column of panels representing a different scaling approach. In the left column, the scalings follow the maximum disk prescription ( $\Gamma = 1, 0.5, 0.25$ , top to bottom). The middle column applies adjustments based on Bell et al. (2003)'s population synthesis models [23]( $\mathcal{P} = 2, 1, 0.5$ , top to bottom), while the right column uses mass-to-light ratios from the MDAcc ( $Q = 2, 1, 0.5$ , top to bottom). It should be noted that setting $\Gamma$ , $\mathcal{P}$ , or $Q$ to zero reproduces the gas-only case. To prevent exceeding the maximum disk limit, galaxies that would otherwise surpass it under the $\mathcal{P}$ or $Q$ scalings are instead plotted at the maximum disk value (denoted by open symbols). Half of the sample already reaches this constraint by $Q = 2$ . For consistency, all panels include a dashed line marking the $Q = 1$ fit as a comparative baseline
4.1 Schematic of the proposed setup. Two balls are of the same radius and density.

The arrow in the left represents a uniform gravitational field. The two spheres are placed such that their symmetry axis is parallel with or perpendicular to the gravitational external field. The effect of external gravity is to pull the two-mass system downward. Due to the mutual gravitational attraction of the two balls, they will slowly move toward each other and finally collide.
4.2 The displacements of two balls
4.3 Graph of velocity versus time calculated using Newtonian mechanics. Two spheres are set to be platinum balls of radius 1cm. The distance between the centers of two balls is 2.0002 cm
4.4 Velocity and Position over time for both internal gravity and air friction cases. Two balls are set to be platinum balls of radius 1cm. The distance between the centers of two balls is $2.0002$ cm. Air viscosity is $1.81 \times 10^{-5}$ Pa×s. Label "Without Air Drag refers to the internal gravity case
4.5 Magnified View of Fig. 4.4 around t = 8s
4.6 Ratio of gravity to air friction over time and value of gravity over time for air friction case
4.7 Notations used to simplify implications of 10 seconds measurement time. The black bar situated in the middle of two balls represents the position where two balls collide. The dashed line is the distance from the edge of one ball to the collision point, denoted as $\epsilon r$ —the distance is expressed as the ball's radius multiplied by a proportionality factor
4.8 Collision time versus ε for platinum ball
4.9 Notation used for rotating coordinate system
4.10 Schematic diagram of spiral motion
4.11 Trajectories of spiral motions with different ratios
4.12 Ratio of internal gravity to Coriolis force
4.13 Trajectory of spiral motion with $k = 1 \times 10^7$

## LIST OF TABLES

4.1	Maximum radius for balls made of various materials	27
4.2	Values of $\epsilon$ and the associated distance between the surface of two-body	
syste	n for the investigated materials	29

#### LIST OF SYMBOLS

G Gravitational constant

ρ Mass densityv Velocity

a Acceleration

m Mass

Φ Gravitational potential

 $\theta$  Angle from the direction of the external field

 $\eta$  Dynamic viscosity

L Lagrangian

a<sub>0</sub> Critical acceleration, m/s<sup>2</sup>

 $M_{\odot}$  Mass of the Sun

 $S_{qrav}$  Gravitational action

 $S_{matter}$  Matter action

 $g_e$  External gravitational field

 $M_{stars}$  Stellar mass in galaxy

 $M_{gas}$  Gaseous mass in galaxy

 $Y_{stars}$  Stellar mass-to-light ratio of stellar disk

 $\Upsilon_{bul}$  Stellar mass-to-light ratio of bulge

CMB Cosmic Microwave Background

WIMPs Weakly Interacting Massive Particles

DAMA Dark Matter

LIBRA Large Sodium Iodide Bulk for Rare Processes

LUX Large Underground Xenon MOND Modified Newtonian Dynamics

EFE External Field Effect

#### **CHAPTER 1**

#### INTRODUCTION

Current astrophysics and cosmology encounter dark matter as one of their most puzzling scientific mysteries. Swiss astronomer Fritz Zwicky discovered the trouble in the 1930s by analyzing behavior in the Coma Cluster [1]. The velocity dispersion results from Zwicky showed that the cluster galaxies maintained motion beyond what could be explained by gravity of ordinary visible matter and proposed dark matter as a possible explanation for cluster stability in his 1933 research.

Research studies conducted after provided various observational evidence that confirms the existence of dark matter. Vera Rubin together with her colleagues performed crucial observations on galactic rotation curves during the 1970s, which remains the most important proof of dark matter existence [2]. Today scientists showed that velocities of stars at the edge of the galaxy did not decrease as stars moved further from the center. Such unexpected gravitational effects in galactic systems require an additional gravitational influence, either undetectable matter or modified gravity. External verification came from CMB temperature fluctuations measurements which gave precise data points. Research on CMB anisotropy reveals that visible matter comprises a small percentage of what makes up the universe [3].

There are different theoretical explanations together with possible candidate particles to explain the origin of dark matter. Interestingly, Weakly Interacting Massive Particles (WIMPs), among all proposed dark matter candidates, have appealing features. The properties of WIMPs match weak nuclear interactions and their predicted number exists in proportions that match the observed density of dark matter in the cosmos. Some authors investigate the axion as another major candidate. Axion is proposed to resolve the strong CP problem and potentially serves as dark matter.

Yet, experimental search for dark matter particle has not been successful. Investigations involving dark matter detection spread across the world and experiments were conducted during the last few decades through DAMA/LIBRA, LUX, and XENON. The detection experiments use multiple technological methods to directly search for signals from dark matter interacting with standard matter. The DAMA/LIBRA research produced questionable signals yet other groups were unable to validate these results and scientists could attribute these results to background noise [4, 5, 6]. In these conditions, modified gravity models gain attention.

Mordehai Milgrom established the MOND (Modified Newtonian Dynamics) theory in his 1983 paper [7]. According to MOND, the gravitational law needs modification at low acceleration. The slow decay rate for gravity predicted by MOND at low acceleration assists scientists in explaining the fast stellar motion in distant galaxy

peripheries without introducing dark matter particle.

At the same time MOND predicts that gravitational fields around systems affect how these systems follow MOND modifications. The way MOND behaves depends on both the strength and orientation of external gravitational fields. This is called the external field effect. The purpose of this project is to calculate experimental conditions to detect EFE and hence test MOND in dedicated precision setup.

#### **CHAPTER 2**

#### DARK MATTER PHENOMENON

#### 2.1 Galactic Rotation Curve

The observational results severely disagree with the predictions of classical Newtonian mechanics based on the distribution of visible matter. This suggests the existence of extra mass, which is called "dark matter".

In classic Newtonian Dynamics, the rotational velocity of a star around galaxy center can be calculated as following:

In central region, assuming the mass density is constant, the mass enclosed by a sphere of radius r is:

$$m(r) = \frac{4}{3}\pi\rho r^3 \tag{2.1.1}$$

In orbital motion of stars, gravity provides the necessary centripetal force:

$$\frac{Gm(r)}{r^2} = \frac{v^2}{r} \tag{2.1.2}$$

Substituting Equation (2.1.1) yields:

$$v(r) = \sqrt{\frac{Gm(r)}{r}} = \sqrt{\frac{4}{3}G\pi\rho} \times r$$
 (2.1.3)

From Equation (2.1.3) we can tell velocity increases linearly with distance: $v(r) \propto r$ 

At the edge of the galaxy, assuming most of the galaxy's mass (M) is concentrated in the core, we then can treat the galaxy as a point mass with mass M. The velocity at large radius is therefore:

$$v(r) = \sqrt{\frac{GM}{r}} \tag{2.1.4}$$

The rotating velocities of stars at the edge of a galaxy is expected to decrease with the square root of distance as we can see in Equation (2.1.4). It turns out that the experimental data does not agree with this expectation as shown in Fig.2.1.

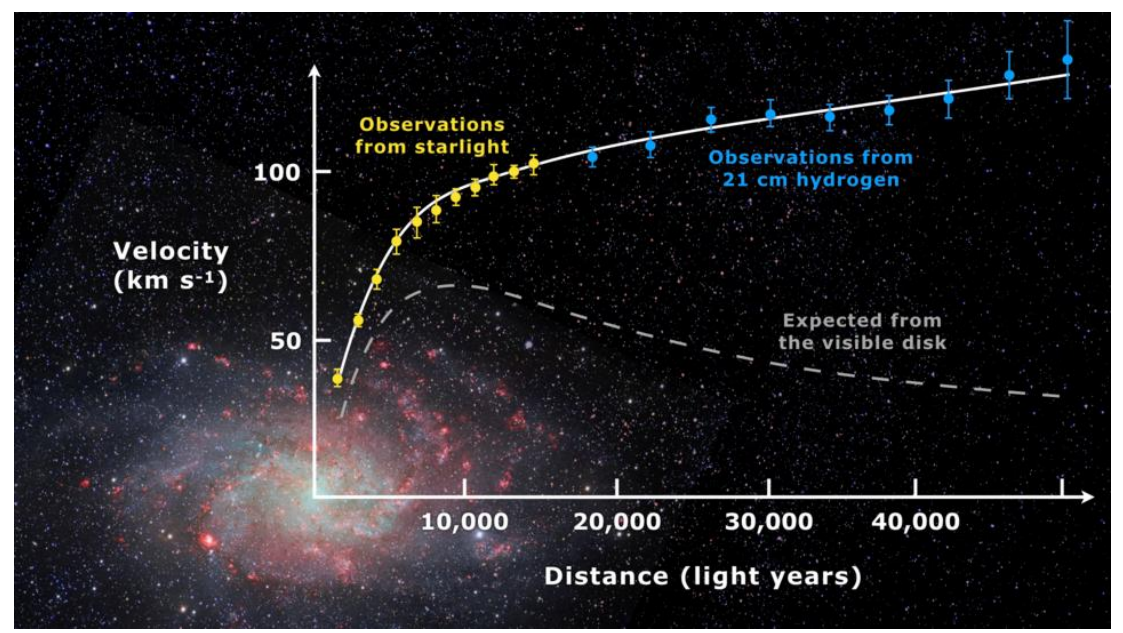


Figure 2.1: Rotation curve of spiral galaxy Messier 33 [8]. The data points of color yellow and blue with error bars is the observational data of stars' speed with respect to the distance from the center of galaxy. The gray dashed line is the theoretically expected rotation curve based solely on the distribution of visible matter. The solid line represents the best fit model of observation data. The x-axis is the radial distance from the galactic center. The origin of x-axis stands for the center of the galaxy (figure from [9]).

The figure demonstrates a comparative assessment of measured rotation curve data along with theoretical predictions that pertain to Messier 33 (M33) spiral galaxy. The work of Edvige Corbelli and Paolo Salucci shows that the stellar velocities remain almost constant—even greater—with increasing radial distance, which is indicative of additional mass distribution—dark matter [8].

#### 2.2 Galaxy Cluster

Compared to galactic rotation curves, galaxy cluster collisions provide more clear and direct evidence for dark matter. In their research, Douglas Clowe et al. constructed gravitational lensing maps of a merging galaxy cluster—the Bullet Cluster 1E 0657-558. The maps clearly show a spatial separation between the cluster's baryonic matter—detected through X-ray emissions—and its total mass distribution—represented by gravitational lensing [10], see Fig. 2.2.

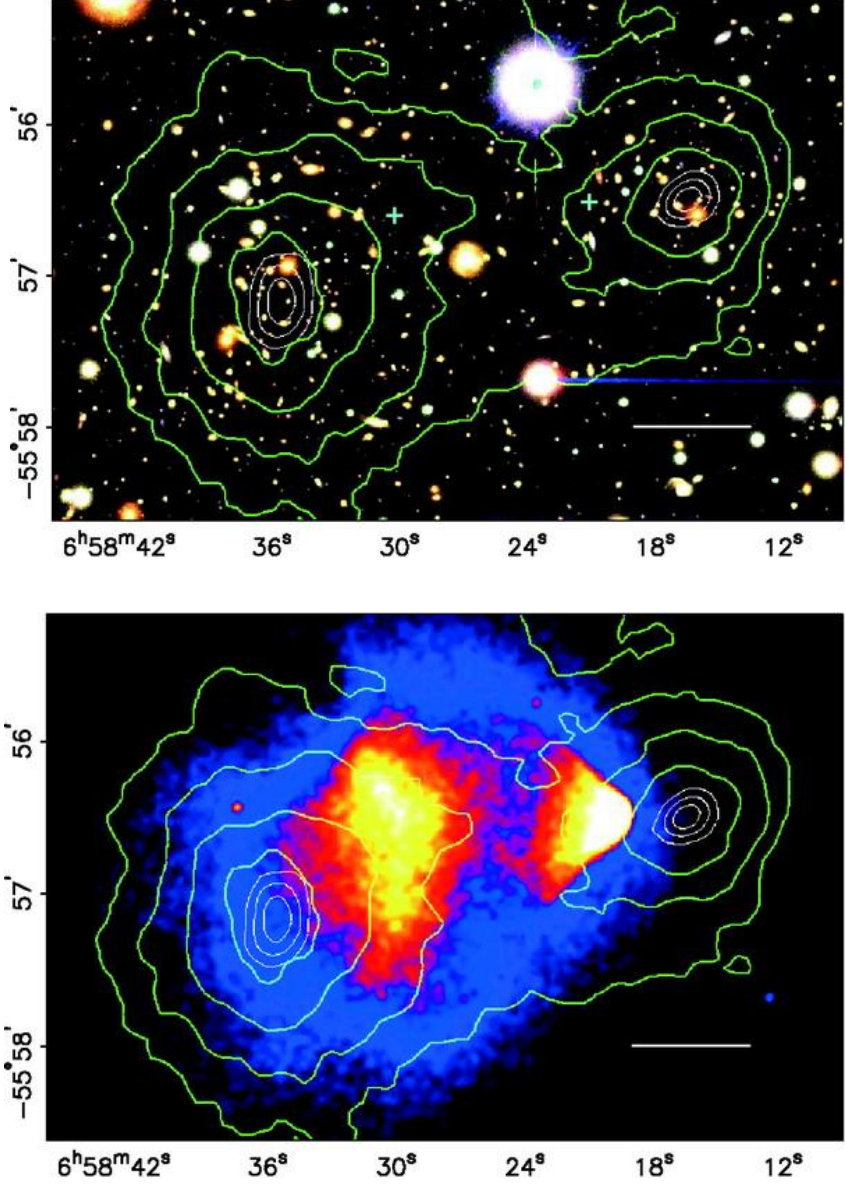


Figure 2.2: X-ray emission and gravitational lensing map of the Bullet Cluster 1E 0657-558. The green contours in top and bottom graphs are the gravitational lensing results. The plus symbol in the pannel on top indicates the centers of masses of plasm clouds. White bars represent distance of 200kpc (figure from [10]).

The colored regions in Fig 2.2 correspond to X-ray plasma, which is the main ingredient of visible matter and the dominant baryonic mass component. We see that the two centers of mass of the merging cluster deviate greatly from the centers of visible matter—plasma cloud.

#### **CHAPTER 3**

#### THEORY OF MOND

#### 3.1 Key Hypotheses of MOND

The essential idea of Modified Newtonian Dynamics (MOND) is based on two fundamental hypotheses that differentiate it from classical Newtonian mechanics and theories that depend on dark matter. These hypotheses were first proposed by Mordehai Milgrom in 1983[7].

Hypothesis 1: Acceleration scale  $a_0$ 

MOND introduces a critical acceleration scale  $a_0 \approx 1.2 \times 10^{-10} \, m/s^2$ , below which gravitational dynamics deviate from Newtonian predictions. This value is empirically determined from galaxy rotation curves. In the deep-MOND regime  $(a \ll a_0)$ , the effective gravitational force becomes:

$$F \approx m \cdot \sqrt{a_0 \cdot g_N} \tag{3.1.1}$$

where  $g_N = Gm/r^2$  is the Newtonian acceleration.

Hypothesis 2: Interpolation function  $\mu(x)$ 

According to MOND theory there exists a continuous shift between classical Newtonian dynamics and MOND that uses an interpolation function  $\mu(x)$  which depends on the ratio  $x = a/a_0$ . The function satisfies:

$$\mu(x) \approx \begin{cases} x & \text{if } x \ll 1 \text{ (Deep MOND Regime)} \\ 1 & \text{if } x \gg 1 \text{ (Newtonian Regime)} \end{cases}$$
(3.1.2)

Commonly used forms are the so-called "standard" function:

$$\mu(x) = \frac{x}{\sqrt{1+x^2}} \tag{3.1.3}$$

And the "simple" function:

$$\mu(x) = \frac{x}{1+x} \tag{3.1.4}$$

This ensures that MOND reduces to Newtonian mechanics at high accelerations ( $a \gg a_0$ ) avoiding conflict with Solar System tests [11].

#### 3.2 Modified Newton's Second Law

MOND proposes a quantitative departure from Newton's second law at extremely low accelerations. One way investigated by Milgrom to achieve that departure is to replace the standard Newton's second law  $F = m \cdot a$  with [12,13]:

$$F = m \cdot \mu \left(\frac{a}{a_0}\right) \cdot a \tag{3.2.1}$$

where m is the mass of the object, a is the acceleration and  $a_0$  is the critical acceleration scale—empirically determined to be  $1.2 \times 10^{-10} \, m/s^2$ . This is to be read that any system (not only gravitational) is subject to modified dynamics.

Now substituting the equation of gravity into Equation. (3.2.1):

$$\frac{GMm}{r^2} = m \cdot \mu \left(\frac{a}{a_0}\right) \cdot a = ma_N \tag{3.2.2}$$

where  $a_N$  is the acceleration calculated in the classical Newtonian dynamics. From Equation. (3.2.2) we can see that the force itself is the same in both MOND and classical Newtonian dynamics. However, it can be considered that there is extra factor in front of mass m. So, the inertial mass which reflects an object's resistance to acceleration is now different from gravitational mass which determines the gravitational force experienced by an object in a gravitational field. Hence, the approach of revising Newton's second law to account for object motion at very low accelerations is called "Modified Inertia".

Taking the standard  $\mu(x)$ , Equation (3.2.2) becomes:

$$a = \sqrt{\frac{a_N^2 + a_N \sqrt{a_N^2 + 4a_0^2}}{2}}$$
 (3.2.3)

In deep MOND regime( $a_N \ll a_0$ ), Equation (3.2.3) becomes:

$$a = \sqrt{a_0 a_N}$$

i.e. it reduces back to Equation (3.2.1).

However, modifications to Newton's second law remain controversial. The core issue stems from violations of fundamental physical principles—such as momentum conservation. In a two-body system, the interaction forces in Newtonian mechanics is

$$F_N = \frac{Gm_1m_2}{(x_2 - x_1)^2}$$

Therefore, the MOND accelerations for  $m_1$  and  $m_2$  are:

$$\begin{cases} a_1 = \sqrt{\frac{F_N a_0}{m_1}} \\ a_2 = \sqrt{\frac{F_N a_0}{m_2}} \end{cases}$$

Then the time derivative of the momentum of the two—body system is:

$$\dot{p} = m_1 \dot{v}_1 + m_2 \dot{v}_2 = m_1 a_1 \hat{x} + m_2 (-a_2 \hat{x}) = \sqrt{F_N a_0} \cdot \left(\sqrt{m_1} - \sqrt{m_2}\right)$$

This causes the system's total momentum to change over time. This non-conservation for an isolated system is a strong agreement against modified inertia.

#### 3.3 Modified Gravity

The conservation problems were solved in the work by Bekenstein and Milgrom [14] by introducing modifications for the gravitational force.

Their formalism (called AQUAL for Aquadratic Lagragian):

$$S_{grav} = -\int \frac{a_0^2}{8\pi G} F\left(\frac{|\nabla \Phi|^2}{a_0^2}\right) d^3x dt$$
 (3.3.1)

where  $\Phi$  is the gravitational potential i.e.  $-\nabla \Phi$  is the MOND acceleration, and F is a dimensionless function.

The matter action (coupling to gravity) is:

$$S_{matter} = -\int \rho \Phi d^3x dt \tag{3.3.2}$$

where  $\rho$  is the mass density. The total action is therefore:

$$S = S_{grav} + S_{matter} (3.3.3)$$

To derive the field equation, we vary the total action with respect to  $\Phi$  and set  $\delta S=0$ . The variation of the gravitational action is:

$$\delta S_{grav} = -\frac{a_0^2}{8\pi G} \int \delta F\left(\frac{|\nabla \Phi|^2}{a_0^2}\right) d^3x dt$$

Applying the chain rule:

$$\delta F = F' \left( \frac{|\nabla \Phi|^2}{a_0^2} \right) \cdot \delta \left( \frac{|\nabla \Phi|^2}{a_0^2} \right) = F' \cdot \frac{2\nabla \Phi \cdot \nabla(\delta \Phi)}{a_0^2}$$

Thus

$$\delta S_{grav} = -\frac{1}{4\pi G} \int F'\left(\frac{|\nabla \Phi|^2}{a_0^2}\right) \nabla \Phi \cdot \nabla (\delta \Phi) d^3x dt$$

Since

$$F'\left(\frac{|\nabla\Phi|^2}{a_0^2}\right)\nabla\Phi\cdot\nabla(\delta\Phi) = \nabla\cdot\left[F'\left(\frac{|\nabla\Phi|^2}{a_0^2}\right)\nabla\Phi\delta\Phi\right] - \nabla\cdot\left[F'\left(\frac{|\nabla\Phi|^2}{a_0^2}\right)\nabla\Phi\right]\delta\Phi$$

 $\delta S_{grav}$  can be written as:

$$\begin{split} \delta S_{grav} &= -\frac{1}{4\pi G} \int \nabla \cdot \left[ F' \left( \frac{|\nabla \Phi|^2}{a_0^2} \right) \nabla \Phi \delta \Phi \right] d^3x dt \\ &+ \frac{1}{4\pi G} \int \nabla \cdot \left[ F' \left( \frac{|\nabla \Phi|^2}{a_0^2} \right) \nabla \Phi \right] \delta \Phi d^3x dt \end{split}$$

According to Gauss's Divergence Theorem, we have:

$$\frac{1}{4\pi G} \int \nabla \cdot \left[ F' \left( \frac{|\nabla \Phi|^2}{a_0^2} \right) \nabla \Phi \delta \Phi \right] d^3x dt = \oint \delta \Phi \left( F' \left( \frac{|\nabla \Phi|^2}{a_0^2} \right) \nabla \Phi \right) \cdot d\mathbf{S}$$

And this term disappears as we assume that  $\delta\Phi$  vanishes at the boundary  $(r \to \infty)$ .

Hence  $\delta S_{grav}$  is

$$\delta S_{grav} = \frac{1}{4\pi G} \int \nabla \cdot \left[ F' \left( \frac{|\nabla \Phi|^2}{a_0^2} \right) \nabla \Phi \right] \delta \Phi d^3 x dt$$

The variation of the matter action is:

$$\delta S_{matter} = -\int \rho \delta \Phi d^3x dt$$

Thus, the variation of total action is:

$$\delta S = \delta S_{grav} + \delta S_{matter}$$

Setting  $\delta S = 0$ , gives:

$$\frac{1}{4\pi G} \nabla \cdot \left[ F' \left( \frac{|\nabla \Phi|^2}{a_0^2} \right) \nabla \Phi \right] \delta \Phi - \rho \delta \Phi = 0 \tag{3.3.4}$$

Rearranging Equation (3.3.4) yields the modified Poisson equation:

$$\nabla \cdot \left[ \mu \left( \frac{|\nabla \Phi|}{a_0} \right) \nabla \Phi \right] = 4\pi G \rho \tag{3.3.5}$$

where  $\mu(x) = F'(x^2)$  is the MOND interpolation function that satisfies asymptotic behavior described as Equation (3.1.2).

In the Newtonian limit ( $|\nabla \Phi| \gg a_0$ ),  $\mu(|\nabla \Phi|/a_0) \approx 1$ , Equation (3.3.5) becomes:

$$\nabla^2 \Phi_N = 4\pi G \rho \tag{3.3.6}$$

In MOND regime ( $|\nabla \Phi| \ll a_0$ ),  $\mu(|\nabla \Phi|/a_0) \approx |\nabla \Phi|/a_0$ , Equation (2.3.5) becomes:

$$\nabla \cdot \left( \frac{|\nabla \Phi|}{a_0} \nabla \Phi \right) = 4\pi G \rho \tag{3.3.7}$$

Substituting Equation (3.3.6) into Equation (3.3.7) gives:

$$\nabla \cdot \left( \frac{|\nabla \Phi|}{a_0} \nabla \Phi \right) = \nabla^2 \Phi_N$$

Hence

$$\nabla \cdot \left( \frac{|\nabla \Phi|}{a_0} \nabla \Phi - \nabla \Phi_N \right) = 0 \tag{3.3.8}$$

Let  $\mathbf{u} = \nabla \Phi_N - \frac{|\nabla \Phi|}{a_0} \nabla \Phi$ . We know from Equation (3.3.8) that the divergence of  $\mathbf{u}$  is zero. So  $\mathbf{u}$  can be expressed as the curl of a vector  $\mathbf{A}$ :

$$\boldsymbol{u} = \nabla \times \boldsymbol{A} \tag{3.3.9}$$

Hence

$$A(r) = \frac{1}{4\pi} \int \frac{\nabla' \times u'(r')}{|r - r'|} d^3 r'$$
 (3.3.10)

Thus we can write the multipole expansion of  $\boldsymbol{u}$  as:

$$\mathbf{u} = -\frac{1}{r^3}(\mathbf{r} \times \mathbf{B}) + 0(r^{-2}) \tag{3.3.11}$$

where  $B = (4\pi)^{-1} \int (\nabla' \times \boldsymbol{u}(\boldsymbol{r}') d^3 r')$ . In Equation (3.3.11), only the monopole term is explicitly written, while the higher-order terms of the multipole expansion are collectively grouped into the remainder of order  $O(r^{-3})$ .

Hence

$$\frac{|\nabla \Phi|}{a_0} \nabla \Phi = \nabla \Phi_N - \boldsymbol{u} = \frac{Gmr + r \times \boldsymbol{B}}{r^3}$$
 (3.3.12)

Taking the absolute value of Equation (3.3.12):

$$|\nabla \Phi| = \frac{\sqrt{a_0} (m^2 G^2 + B^2 (\sin \theta)^2)^{\frac{1}{4}}}{r}$$
 (3.3.13)

where  $\theta$  is the angle between **r** and **B**.

Substituting Equation (3.3.13) into Equation (3.3.12):

$$\nabla \Phi = \frac{\sqrt{a_0}}{r^2} \cdot \frac{mGr + r \times B}{(m^2 G^2 + B^2 (\sin \theta)^2)^{\frac{1}{4}}} + O(r^{-2})$$
(3.3.14)

The requirement that  $\nabla \times (\nabla \Phi) = 0$  gives  $\mathbf{B} = 0$ . By setting B to zero and substituting back into Equation (3.3.11), we obtain:

$$u = 0 + O(r^{-3})$$

In the deep-MOND regime (i.e., the low-acceleration limit), when higher-order terms  $O(r^{-3})$  are neglected, u approximately vanishes. This leads to:

$$\frac{|\nabla \Phi|}{a_0} \nabla \Phi - \nabla \Phi_N = 0 \to \frac{|\nabla \Phi|}{a_0} \nabla \Phi = \nabla \Phi_N$$

$$\nabla \Phi = \frac{\sqrt{a_0}}{r^2} \cdot \frac{mGr}{(m^2 G^2)^{\frac{1}{4}}} + O(r^{-2}) = \sqrt{g_N a_0}$$
(3.3.15)

which are precisely the central equations in the section on Modified Newton's Second Law. However, the derivation shows that Equation (3.2.2) is only applicable under certain low-acceleration conditions, indicating its limited use and that it is not a general dynamical equation.

We can also find out that when we get to very large distances from an object of mass M in a vacuum, the gravitational acceleration levels off to far below  $a_0$  (enters deep-MOND regime). In this limit, the isopotentials, will eventually be reaching a spherical symmetry and the curl field will be reduced to zero. Hence the gravitational potential is:

$$\Phi(r) = \sqrt{GMa_0} \ln r \qquad (r \to \infty)(3.3.16)$$

Note that MOND satisfies the Weak Equivalence Principle: All uncharged, freely falling test particles follow the same trajectories, once an initial position and velocity have been prescribed [15]. The center-of-mass acceleration of a low-mass system (e.g., a globular cluster in the Galactic outskirts) is mass-dependent, not structure-dependent even if its constituents undergo internal accelerations above  $a_0$ . Therefore, the collective motion of the system can still adhere to MOND dynamics, even with internal Newtonian behavior.

#### 3.4 Interpolating Functions

The MOND framework only requires  $\mu(x)$  to follow the asymptotic behaviours given by equation (3.1.2) strictly: tending to a unity in the Newtonian regime (x $\gg$ 1), and almost equating x in the deep-MOND regime (x $\ll$ 1). To ensure uniqueness of physical mapping between g and  $g_N$ , there is a necessary condition that x $\mu(x)$  has to be strictly monotonically increasing, i.e.,  $d[x\mu(x)]/dx > 0$ :

$$\mu(x) + x\mu'(x) > 0$$

It can also be written as:

$$\frac{d\ln\mu}{d\ln x} > -1$$

Just how the interpolating function is shaped is not completely fixed which led to the creation of several families of interpolation functions.

First of all, let us note that MOND interpolating function  $\mu(x)$  can also be represented by another function:

$$v(y) = 1/\mu(x) \tag{3.4.1}$$

Where  $y = x\mu(x)$ . In this case, the function  $y\nu(y)$  must increase steadily with every increase in y

To demonstrate how interpolating functions are transformed, an example is presented that details the mathematics used to get from  $\mu(x)$  to  $\nu(y)$ .

The simple  $\mu$ -function is written as:

$$\mu(x) = \frac{x}{1+x} \tag{3.4.4}$$

Therefore,  $y = x^2/(1+x)$  and one verifies that

$$x^2 - yx - y = 0$$

The root value of x is

$$x = \frac{y \pm \sqrt{y^2 + 4y}}{2}$$

Since x is the ratio of acceleration to characteristic acceleration  $a_0$ . It cannot take a negative value. Hence

$$\chi = \frac{y + \sqrt{y^2 + 4y}}{2} \tag{3.4.5}$$

Then, Equation (3.4.1) and Equation (3.4.5) gives the simple  $\nu$ -function

$$\nu(y) = \frac{1 + \sqrt{1 + \frac{4}{y}}}{2} \tag{3.4.6}$$

We would like to propose a new class interpolating functions, parameterized with a real number  $n \ge 0$ . This is motivated by the setup aimed at testing EFE. Our function reads:

$$\mu_n(x) = \frac{x}{(1+x^n)^{1/n}} \tag{3.4.11}$$

When n=1, it is the simple  $\mu$ -function, While, when n=2 it becomes the standard  $\mu$ -function. The corresponding  $\nu$ -function is of the form:

$$\nu_n(y) = \left[\frac{1 + \sqrt{1 + \frac{4}{y^n}}}{2}\right]^{\frac{1}{n}}$$
(3.4.12)

An example of other families of functions was given in [16]:

$$\nu_m(y) = \frac{1}{\sqrt{1 - \frac{1}{e^y}}} + \frac{m}{e^y}$$
 (3.4.13)

$$\nu_n(y) = \left(1 - e^{-y^{n/2}}\right)^{-1/n} + (1 - \gamma^{-1})e^{-y^{n/2}}$$
(3.4.14)

Summing up, we wanted to highlight the range of theoretical choices available in the interpolating function of MOND. In order to accurately decide its detailed shape, the data from galaxy rotation curves must be extremely accurate. Still, some uncertainty in measurements of distance and mass-to-light ratios (or from studies of purely gaseous galaxies) might be present. Data from today's solar spacecraft mostly prefer simple function [17] or interpolation function between n=1 and n=2 in Equation (3.4.11). Fig. 3.1 visually compares examples of the discussed functions. They all show alike behaviors in the MONND regime and differ for  $a/a_0 > 1$ .

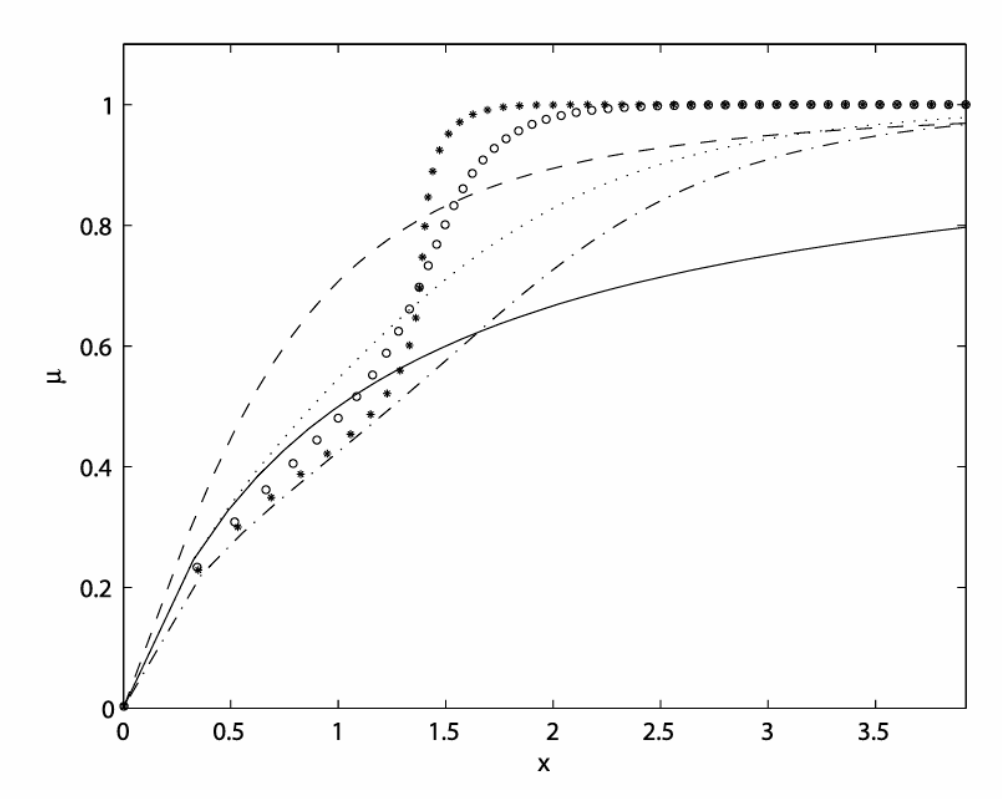


Figure 3.1: Comparison of different  $\mu$ -function profiles as a function of x—the ratio of acceleration to the characteristic acceleration scale  $a_0$ . The solid line and dashed line are the plots of Equation (3.4.11), with n=1 (simple  $\mu$ -function) and n=2 (standard  $\mu$ -function), respectively. Dotted line and dashed-dotted line are curves of Equation (3.4.13) for m=0.5 and m=1 respectively. The circular marker line and starred marker line depicts Equation (3.4.14) with n=4 and n=6 respectively (figure from [16]).

#### 3.5 The External Field Effect

While Newtonian dynamics and general relativity ensure that subsystems are not affected by uniform, homogeneous external fields, MOND proposes that the way galaxies move is influenced most by the total gravitational acceleration. Essentially, MOND can be seen when both g and  $g_e$  accelerations fall under the threshold  $a_0$ . For  $g < a_0 < g_e$ , Newtonian theory is used as normal; and for  $g < g_e < a_0$ , the gravitational constant in Newtonian dynamics is modified. Whenever g becomes less

than  $g_e$ , the gravitational pull always returns to its customary  $1/r^2$  law, but with an angular dependence

The following text will delve into how to derive the specific formulas for calculating the external field effect, starting from the basic principles of MOND.

Suppose we first have a solution  $\phi_e(\vec{r})$  to the modified Poisson equation for a large mass distribution  $\rho_e$ .

Now we add a small mass distribution  $\rho_r$  to its vicinity. The total gravitational potential at an arbitrary point P due to these two mass distributions is  $\Phi$ . We assume the gravity due to  $\rho_r$  is sufficiently weak such that the total gravitational force is a small perturbation to  $\nabla \Phi$ :

$$\vec{\nabla}\Phi = \vec{\nabla}\phi_{\rho} + \vec{\nabla}\varphi \tag{3.5.1}$$

where  $\varphi$  is the gravitational potential of  $\rho_r$ 

Now expand  $\frac{|\vec{\nabla}\Phi|}{a_0}$  about  $\frac{|\vec{\nabla}\phi_e|}{a_0}$ :

$$\frac{|\vec{\nabla}\Phi|}{a_0} = \frac{a_e}{a_0} - \frac{\vec{a_e}}{a_0 a_e} \cdot \vec{\nabla}\varphi \tag{3.5.2}$$

where  $\overrightarrow{a_e} = -\overrightarrow{\nabla}\phi_e$  and  $a_e = |\overrightarrow{\nabla}\Phi|$ . Neglecting all terms with order of  $\overrightarrow{\nabla}\varphi$  higher than one since  $\overrightarrow{\nabla}\varphi$  is weak.

Then, expand the interpolating function about  $a_e/a_0$ :

$$\mu\left(\frac{|\vec{\nabla}\Phi|}{a_0}\right) = \mu\left(\frac{a_e}{a_0} - \frac{\overrightarrow{a_e}}{a_0a_e} \cdot \overrightarrow{\nabla}\varphi\right) = \mu\left(\frac{a_e}{a_0}\right) - \mu'\left(\frac{a_e}{a_0}\right) \frac{\overrightarrow{a_e}}{a_0a_e} \cdot \overrightarrow{\nabla}\varphi \tag{3.5.3}$$

Let  $\mu_e = \mu\left(\frac{a_e}{a_0}\right)$  and  $\mu'_e = \mu'\left(\frac{a_e}{a_0}\right)$ , equation (3.5.3) becomes:

$$\mu\left(\frac{|\vec{\nabla}\Phi|}{a_0}\right) = \mu_e - \mu'_e \frac{\overrightarrow{a_e}}{a_0 a_e} \cdot \overrightarrow{\nabla}\varphi \tag{3.5.4}$$

From equation (3.5.1) and (3.5.4)

$$\mu\left(\frac{\left|\vec{\nabla}\Phi\right|}{a_0}\right)\vec{\nabla}\Phi = \left(\mu_e - \mu_e'\frac{\overrightarrow{a_e}}{a_0a_e}\cdot\vec{\nabla}\varphi\right)\left(\vec{\nabla}\phi_e + \vec{\nabla}\varphi\right)$$
$$= \mu_e\vec{\nabla}\phi_e + \mu_e\vec{\nabla}\varphi - \mu_e'\frac{\overrightarrow{a_e}}{a_0a_e}\cdot\vec{\nabla}\varphi\vec{\nabla}\phi_e$$

Hence

$$\vec{\nabla} \left( \mu \left( \frac{|\vec{\nabla} \Phi|}{a_0} \right) \vec{\nabla} \Phi \right) = \vec{\nabla} \left( \mu_e \vec{\nabla} \phi_e \right) + \vec{\nabla} \left( \mu_e \vec{\nabla} \varphi \right) - \vec{\nabla} \left( \mu'_e \frac{\overrightarrow{a_e}}{a_0 a_e} \cdot \vec{\nabla} \varphi \vec{\nabla} \phi_e \right)$$
(3.5.5)

Simplifying equation (3.5.5) by using equation (3.3.5)

$$4\pi G(\rho_e + \rho_r) = 4\pi G \rho_e + \vec{\nabla} \left(\mu_e \vec{\nabla} \varphi\right) - \vec{\nabla} \left(\mu'_e \frac{\vec{a_e}}{a_0 a_e} \cdot \vec{\nabla} \varphi \vec{\nabla} \phi_e\right)$$

Hence

$$4\pi G \rho_r = \vec{\nabla} \left( \mu_e \vec{\nabla} \varphi \right) - \vec{\nabla} \left( \mu'_e \frac{\overrightarrow{a_e}}{a_0 a_e} \cdot \vec{\nabla} \varphi \vec{\nabla} \phi_e \right) \tag{3.5.6}$$

Suppose the external field is uniform along direction  $\hat{n}$ 

$$\overrightarrow{a_{\rho}} = -\overrightarrow{\nabla}\phi_{\rho} = a_{\rho}\hat{n}$$

Then equation (3.5.6) becomes:

$$4\pi G \rho_r = \vec{\nabla} \left( \mu_e \vec{\nabla} \varphi \right) + \vec{\nabla} \left( \mu_e' \frac{a_e}{a_0} \hat{n} \cdot \vec{\nabla} \varphi \hat{n} \right) = \vec{\nabla} \left( \mu_e \left( \vec{\nabla} \varphi + \frac{\mu_e' a_e}{\mu_e a_0} \hat{n} \cdot \vec{\nabla} \varphi \hat{n} \right) \right) (3.5.7)$$

Now consider  $\rho_r$  is a spherically—symmetric distribution. We choose a spherical coordinate system centered at  $\rho_r$ , with  $\hat{n} = \hat{k}$  along the z-axis. Then

$$\hat{n} = \cos\theta \, \hat{r} - \sin\theta \, \hat{\theta} = \hat{k}$$

Let V be the volume of a ball centered at  $\rho_r$  with radius r:

$$4\pi G \int_{V} \rho_{r} \, dV = \int_{V} \overrightarrow{\nabla} \left( \mu_{e} \left( \overrightarrow{\nabla} \varphi + \frac{\mu'_{e} \, a_{e}}{\mu_{e} \, a_{0}} \, \hat{n} \cdot \overrightarrow{\nabla} \varphi \, \hat{n} \right) \right) dV$$

$$4\pi G M = \int_{\partial V} \left( \mu_{e} \left( \overrightarrow{\nabla} \varphi + \frac{\mu'_{e} \, a_{e}}{\mu_{e} \, a_{0}} \, \hat{n} \cdot \overrightarrow{\nabla} \varphi \, \hat{n} \right) \right) d\vec{\Sigma}$$

where  $d\vec{\Sigma} = r^2 \sin\theta \ d\theta \ d\phi \ \hat{r}$ , here  $\phi$  is the angle in spherical coordinate system.

Then

$$\frac{4\pi GM}{\mu_e} = \int_{\partial V} r^2 \sin\theta \, d\theta d\phi \, \hat{r} \cdot \vec{\nabla} \varphi 
+ \frac{\mu'_e \, a_e}{\mu_e \, a_0} \int_{\partial V} r^2 \sin\theta \, d\theta d\phi \, (\hat{n} \cdot \vec{\nabla} \varphi) (\hat{r} \cdot \hat{n})$$
(3.5.8)

The solution to equation (3.5.8) is [18]:

$$\varphi = -\frac{GM}{\mu_e r \sqrt{1 + \lambda_e sin^2 \theta}} \tag{3.5.9}$$

where  $\mu_e = \mu(y_e)$ ,  $\lambda_e = y_e \,\mu'_e/\mu_e$ ,  $\mu'_e = d\mu(y_e)/dy_e$  and  $y_e = g_e/a_0$ .  $\theta$  is the azimuthal angle from the direction of the external field  $g_e$ . Equation (3.5.9) is similar to  $\varphi = GM/r$ , except that the gravitational constant in Equation (3.5.9) has been

modified: $G_{eff} = G/\mu_e \sqrt{1 + \lambda_e \sin^2 \theta}$ .

#### 3.6 Successes of MOND

#### 3.6.1 Galaxy Rotation Curve

The rotation curve of spiral galaxies can be used as an important test for MOND. If dark matter is left out, astronomers should be able to use the observable matter to predict the rotation curve for galaxies.

The visible matter of galaxy can be categorized into three components: Gas Disk, Stellar Disk and Bulge. The rotational velocities provided by these mass distributions are:

$$V_{stars}^{2}(r) = \frac{GM_{stars}(r)}{r}$$
 (3.6.1)

where  $M_{stars}(r)$  is the stellar mass within sphere of radius r in the disk of the galaxy, and

$$V_{gas}^{2}(r) = \frac{GM_{gas}(r)}{r}$$
 (3.6.2)

Note that the gas component may not be exactly in the shape of a disk. Its 3D mass distribution may be considered.

The total velocity derived from visible matter is [19]:

$$V_N(r) = \sqrt{|V_{gas}|V_{gas} + \Upsilon_{stars}|V_{stars}|V_{stars} + \Upsilon_{bul}|V_{vul}|V_{vul}|}$$
(3.6.3)

where  $Y_{stars}$  and  $Y_{bul}$  is the stellar mass-to-light ratios of stellar disk and bulge, respectively.

Then incorporating Equation (3.6.3),  $a = V^2/r$ ,  $a_N = V_N^2/r$  into Equation (3.2.2) gives:

$$\mu \left(\frac{V^2}{ra_0}\right) \frac{V^2}{r} = \frac{V_N^2}{r} \tag{3.6.4}$$

By applying the simple  $\mu$  function, we have:

$$V = V_N \sqrt{\frac{1 + \sqrt{1 + 4a_0 r V_N^{-2}}}{2}}$$
 (3.6.5)

By applying Equation (3.4.11), we have:

$$V = V_N \left( \frac{1 + \sqrt{1 + 4(ra_0 V_N^{-2})^n}}{2} \right)^{1/2n}$$
 (3.6.6)

To fit the observed rotational velocity profile, we perform a least squares optimization on Equation (3.6.6), treating the mass-to-light ratio as a free parameter that varies within a physically reasonable range.

Begeman, Broeills and Sanders performed an analysis in 1991 and discovered that the rotational speed calculated in MOND was close to the actual rotational speed observed in ten spiral galaxies [20]. In 2012, Benoit Famaey discussed in detail the fitting of Monte Carlo simulations into the rotation curves of different types of galaxies, including High Surface Brightness (HSB), Low Surface Brightness (LSB), spiral, massive and dwarf galaxies [11]. According to Lelli, McGaugh and Schombert, MOND succeeded in predicting how 175 galaxies rotate, without any need for adjustable parameters at the low-acceleration area [19]. Figure 2.2 shows the result from Benoit Famaey.

#### 3.6.2 Tully-Fisher Relation

The Tully-Fisher relation shows that the brightness and rotation velocity of disk galaxies are related to one another. It was first introduced in 1977 by R. Brent Tully and J. Richard Fisher [21] and is now widely used for measuring distances between galaxies as well as in topics related to cosmology. The Tully-Fisher relation is typically expressed as:

$$L \propto V_{max}^{\alpha} \tag{3.6.7}$$

where L is the total luminosity of the galaxy (often measured in infrared or radio wavelengths to minimize dust absorption effects),  $V_{max}$  is the maximum rotational velocity of the galaxy's rotation curve (usually derived from neutral hydrogen 21 cm line or optical spectroscopy),  $\alpha$  is an exponent, typically ranging between 3 and 4 (depending on the observational band).

Equation (3.6.7) can be understood in a simple way within the MOND model. The speed at which a spiral galaxy rotates majorly depends on its gravity which is

influenced by dark matter and ordinary matter. Also, if galaxies have a relatively constant mass-to-light ratio (M/L), then their luminosity L increases in proportion to how much mass they contain. Newtonian mechanics suggests that rotational velocity  $V_{max}$  is proportional to the total mass M much like Kepler's law, where  $V \propto \sqrt{M/R}$ . The integrated equations give us equation (3.6.7), in which the value of  $\alpha$  depends on the mass distribution and its mass-to-light ratio.

As illustrated in Figure 2.1, the maximum rotational velocity of a spiral galaxy occurs in regions far from its center. According to Modified Newtonian Dynamics (MOND), the acceleration of an object at large distances from a mass M is given by

$$a = \sqrt{a_0 a_N}$$

For an object in circular motion, the centripetal acceleration is

$$a = \frac{V^2}{R}$$

Combining these relations, we derive the maximum rotational velocity of a spiral galaxy as follows:

$$V_{max}^4 = GMa_0 \tag{3.6.8}$$

Hence

$$V_{max}^4 \propto M \tag{3.6.9}$$

Then we plug in  $L \propto M$  with the assumption that the mass-to-light ratio (M/L) of a galaxy is relatively constant.

$$L \propto M \propto V^4 \tag{3.6.10}$$

This is the Tully-Fisher relation with  $\alpha = 4$ .

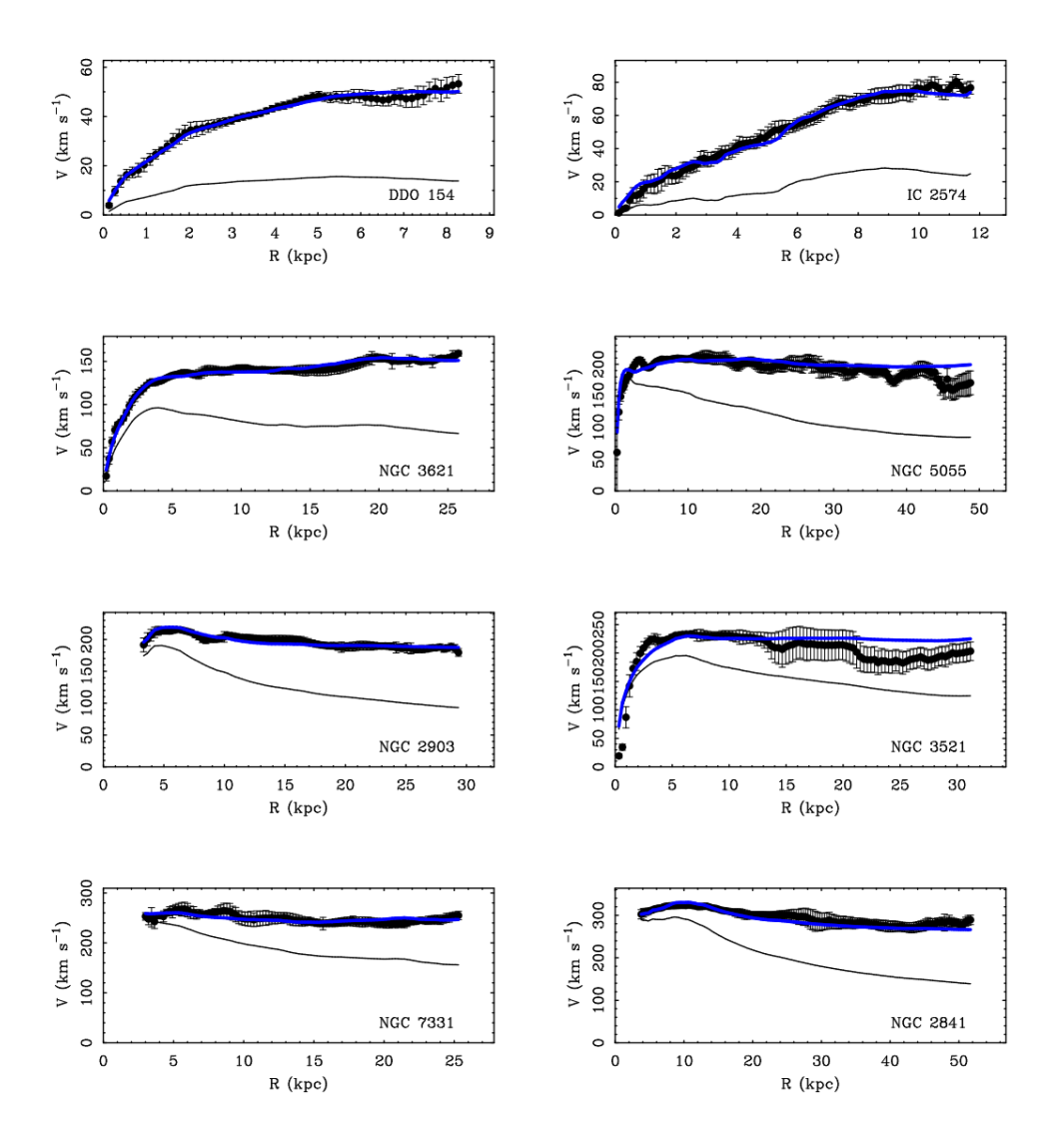


Figure 3.2: MOND rotation curve fits for representative galaxies from the THINGS survey [22]. The baryonic mass of selected galaxies varies from  $3 \times 10^8 M_{\odot}$  to  $3 \times 10^{11} M_{\odot}$ . High-resolution interferometric 21 cm observations are available for the gaseous components of all galaxies, along with 3.6-micron photometric data to map their stellar distributions. Black line is calculated from Newtonian baryonic mass model. Blue is fit curve of MOND. The interpolating function used in the fitting curve is Equation (3.4.14) with n = 1 (figure from [11]).

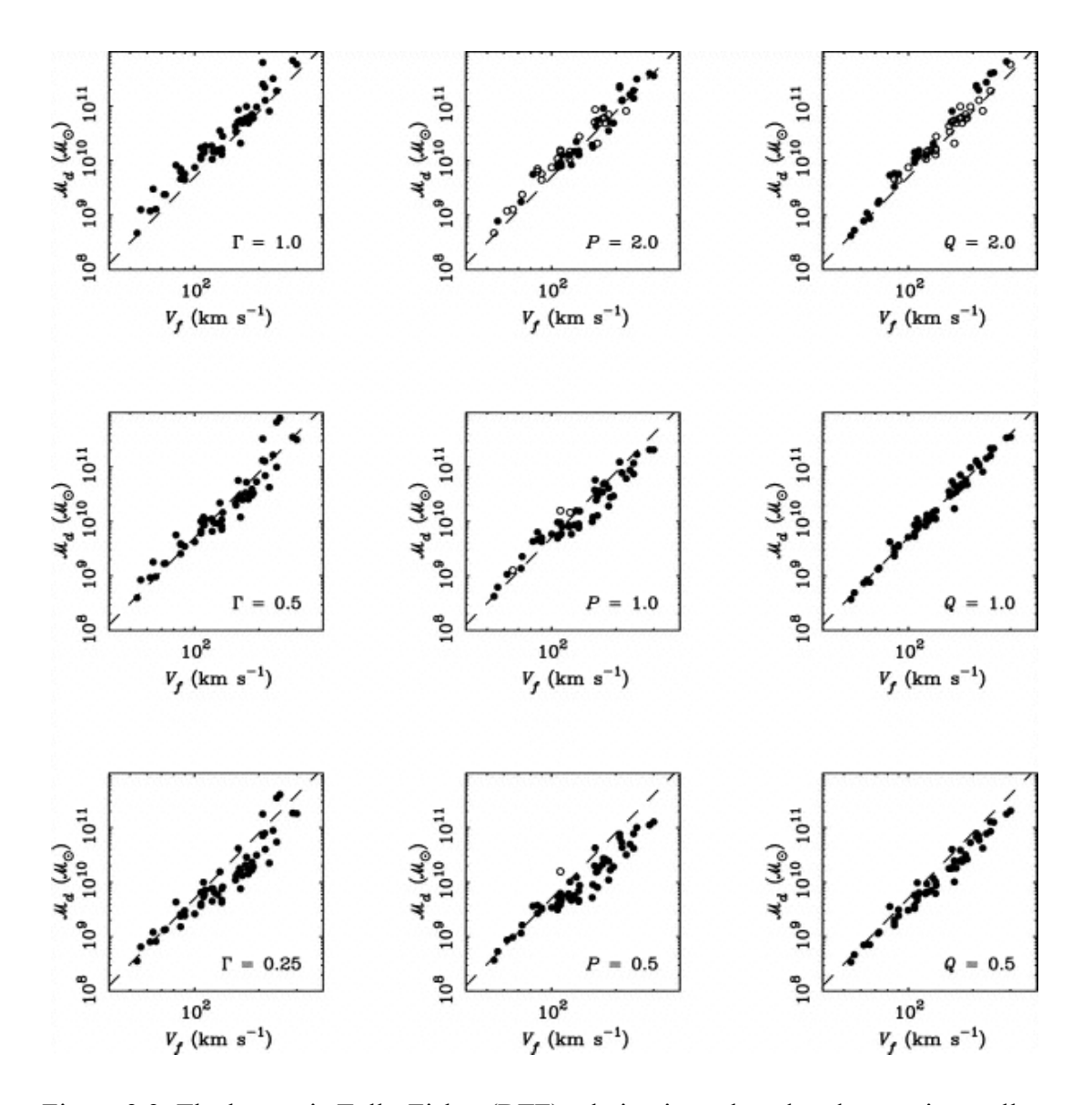


Figure 3.3: The baryonic Tully-Fisher (BTF) relation is analyzed under varying stellar mass-to-light ratio assumptions, with each column of panels representing a different scaling approach. In the left column, the scalings follow the maximum disk prescription ( $\Gamma=1,0.5,0.25$ , top to bottom). The middle column applies adjustments based on Bell et al. (2003)'s population synthesis models [23] ( $\mathcal{P}=2,1,0.5$ , top to bottom), while the right column uses mass-to-light ratios from the MDAcc (Q=2,1,0.5, top to bottom). It should be noted that setting  $\Gamma$ ,  $\mathcal{P}$ , or  $\mathcal{Q}$  to zero reproduces the gas-only case. To prevent exceeding the maximum disk limit, galaxies that would otherwise surpass it under the  $\mathcal{P}$  or  $\mathcal{Q}$  scalings are instead plotted at the maximum disk value (denoted by open symbols). Half of the sample already reaches this constraint by  $\mathcal{Q}=2$ . For consistency, all panels include a dashed line marking the  $\mathcal{Q}=1$  fit as a comparative baseline (figure from [24]).

#### **CHAPTER 4**

#### PROPOSED EXPERIMENT

The EFE is simplest to check on a two-body system embedded into external field. We therefore propose a test with two massive spheres with the axis joining their centers aligned either parallel or orthogonal to the external field, see Fig. 4.1. The parameter we wish to study for revealing different dynamics is the collision time. Recall that under Newton's laws, it is impossible for any such discrepancy to happen. The reason is that, in Newtonian physics, the gravitational field accelerates the entire system and both balls the same way without making them move differently relative to one another. As a result, both of the collisions are predicted to take the same time. The same is predicted by general relativity. Note that uniform external field is removed in the frame accelerating downwards with  $a = g_{ex}$ . From equivalence between acceleration and gravity, the two configurations evolve in exactly the same way.

However, as explained in the last section, in the MOND model we expect to see a difference and we wish to work out how small that difference is.

# 

Figure 4.1 Schematic of the proposed setup. Two balls are of the same radius and density. The arrow in the left represents a uniform gravitational field. The two spheres are placed such that their symmetry axis is parallel with or perpendicular to the gravitational external field. The effect of external gravity is to pull the two-mass system downward. Due to the mutual gravitational attraction of the two balls, they will slowly move toward each other and finally collide.

Since, according to Blanchet and Novak, the only change in the internal system is the effective Newton's constant (if the masses are sufficiently far apart), we start with computing the Newtonian trajectory for the two spheres.

From Energy Conservation Law:

$$\frac{Gm^2}{L-2x} - \frac{Gm^2}{L} = mv^2 \tag{4.1.1}$$

where x is the displacement of one ball, m is the mass of one ball, L is the initial distance between two balls and G is the gravitational constant, see Fig. 4.2.

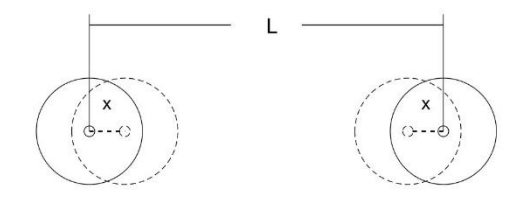


Figure 4.2 The displacements of two balls.

Writing v = dx/dt, Equation (4.1.1) can be written as:

$$dt = \frac{dx}{\sqrt{\frac{Gm}{L-2x} - \frac{Gm}{L}}}$$
 (4.1.2)

After integrating:

$$t = \sqrt{\frac{L}{2Gm}} \left( \sqrt{x(L - 2x)} + \frac{L\sqrt{2}\tan^{-1}(\frac{2x}{L - 2x})}{2} \right)$$
 (4.1.3)

Equation (4.1.3) shows the relationship between time t and ball displacement x.

The collision time is found by putting  $x = \frac{L}{2}$ . If we take balls of radius 1cm and mass 0.0883kg, separated by distance 2.0002 cm, Fig3.3 shows that they will collide at time t  $\approx 12$ s, and the maximum speed of the ball is 1.2 nm/s, which is of a very small value.

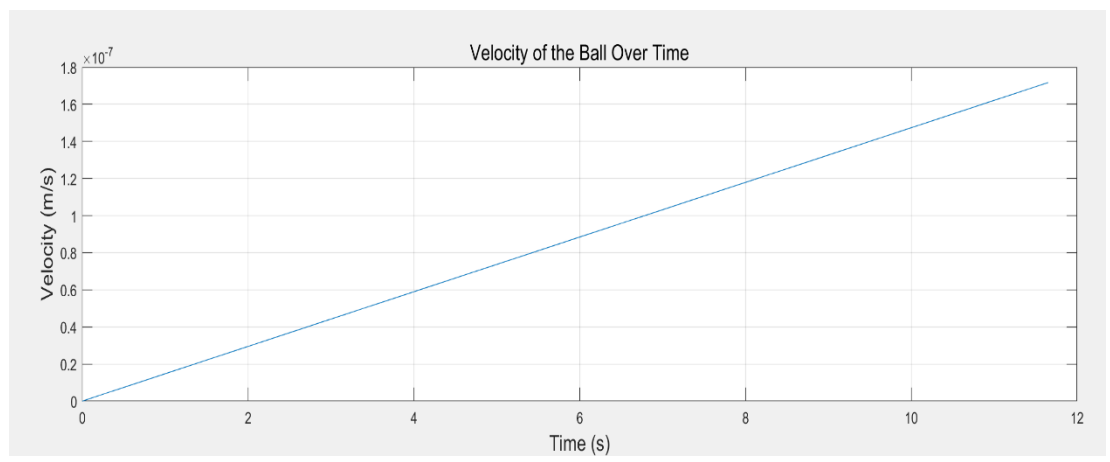


Figure 4.3 Graph of velocity versus time calculated using Newtonian mechanics. Two spheres are set to be platinum balls of radius 1cm. The distance between the centers of two balls is 2.0002 cm.

#### 4.2 Air Friction

To be more realistic we add air friction to the two balls system. As shown in Fig. 4.3, the speeds of two balls are very small throughout the collision process. With the consideration of air drag force, the velocities of two balls will only become smaller than before. The air friction is written as [25]:

$$F = 6\eta \pi r v \tag{4.2.1}$$

where  $\eta$  is the dynamic viscosity of air, r is the ball radius and v is the relative velocity.

From Newton's second law:

$$m\frac{dv}{dt} = \frac{Gm^2}{(L-2x)^2} - 6\eta\pi rv$$
 (4.2.2)

However, due to the difficulty of nonlinear ordinary differential equation, we cannot obtain an analytical solution. One can still calculate the ball displacement and ball velocity at any given time using numerical methods. In this project 4th Order Runge-Kutta method is chosen to calculate the ball displacement and ball velocity. For the detailed code, please refer to the appendix.

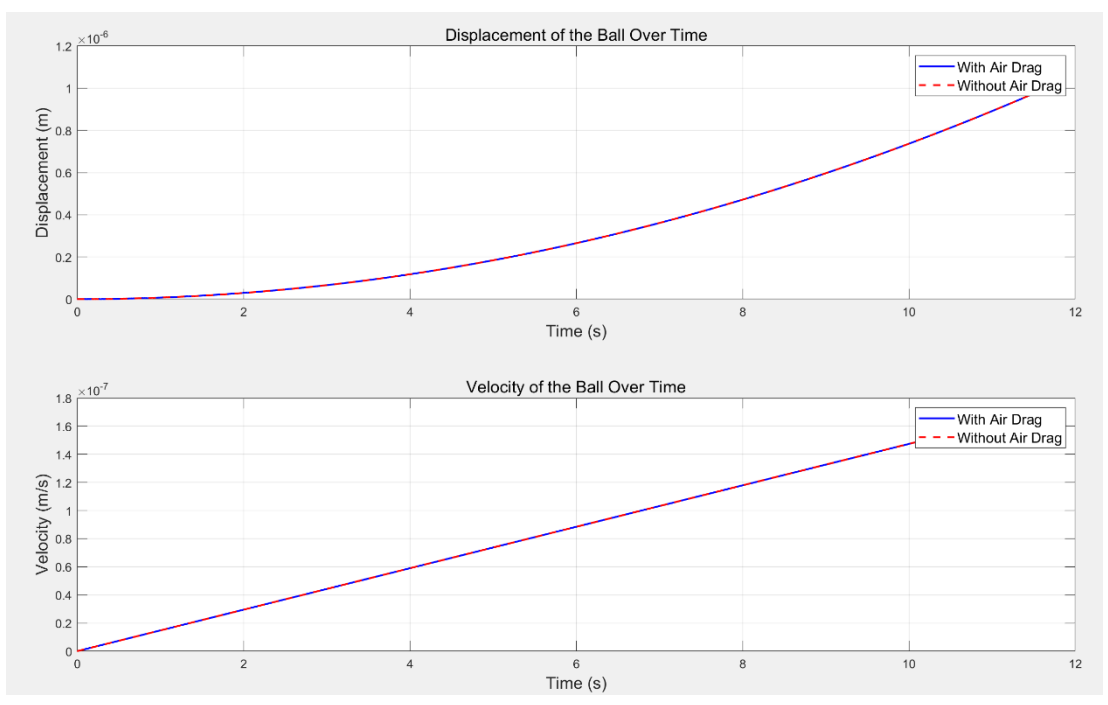


Figure 4.4 Velocity and Position over time for both internal gravity and air friction cases. Two balls are set to be platinum balls of radius 1cm. The distance between the centers of two balls is 2.0002 cm. Air viscosity is  $1.81 \times 10^{-5}$  Pa×s. Label "Without Air Drag" refers to the internal gravity case.

Fig. 4.4 shows that the motion of two balls under air friction case is almost identical to their motion under internal gravity only case. By magnifying the image as shown in Fig. 4.5, one can observe that the motion of two balls shows slight differences under the two conditions, but they are negligible of gravity to air friction

From the upper panel of Fig. 4.6, one can see that the ratio is greater than two thousand. As value of time t becomes smaller and smaller, the ratio increases rapidly. In fact, the reason for the author to plot the ratio from t = 2s is to avoid the influence of extremely big values from time interval [0s,2s], otherwise the shape of the ratio curve is simply "L".

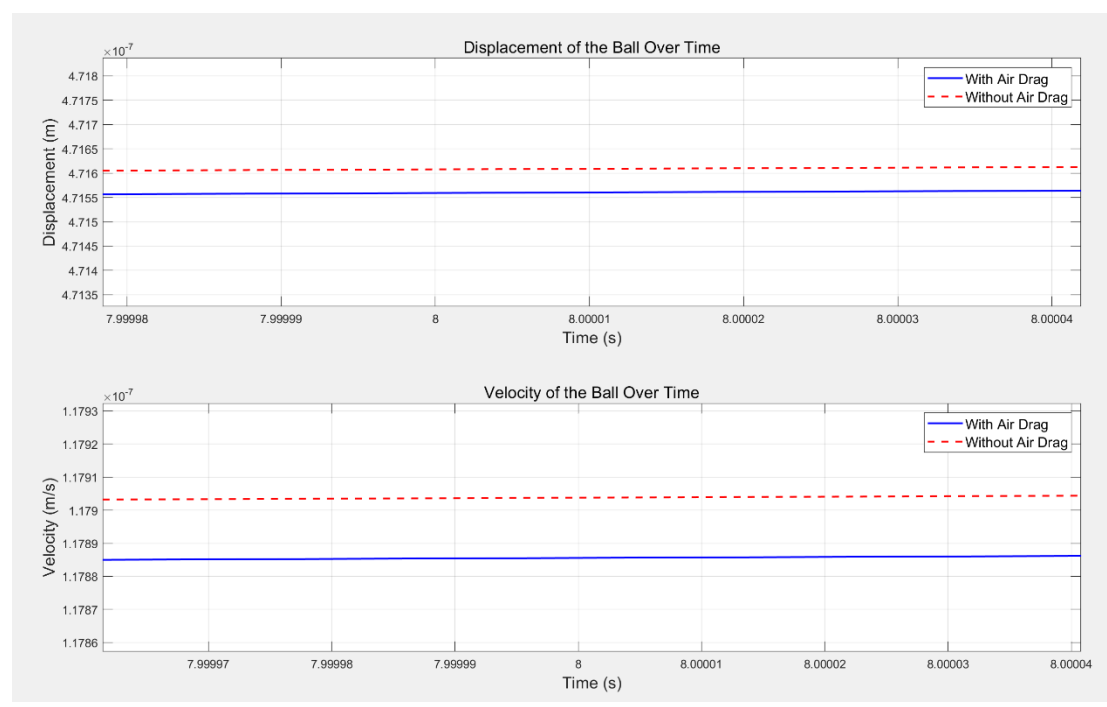


Figure 4.5 Magnified View of Fig. 4.4 around t = 8s.

The reason for the high similarity of motion of two balls under two conditions is that internal gravity dominates the collision process of two balls in air friction case.

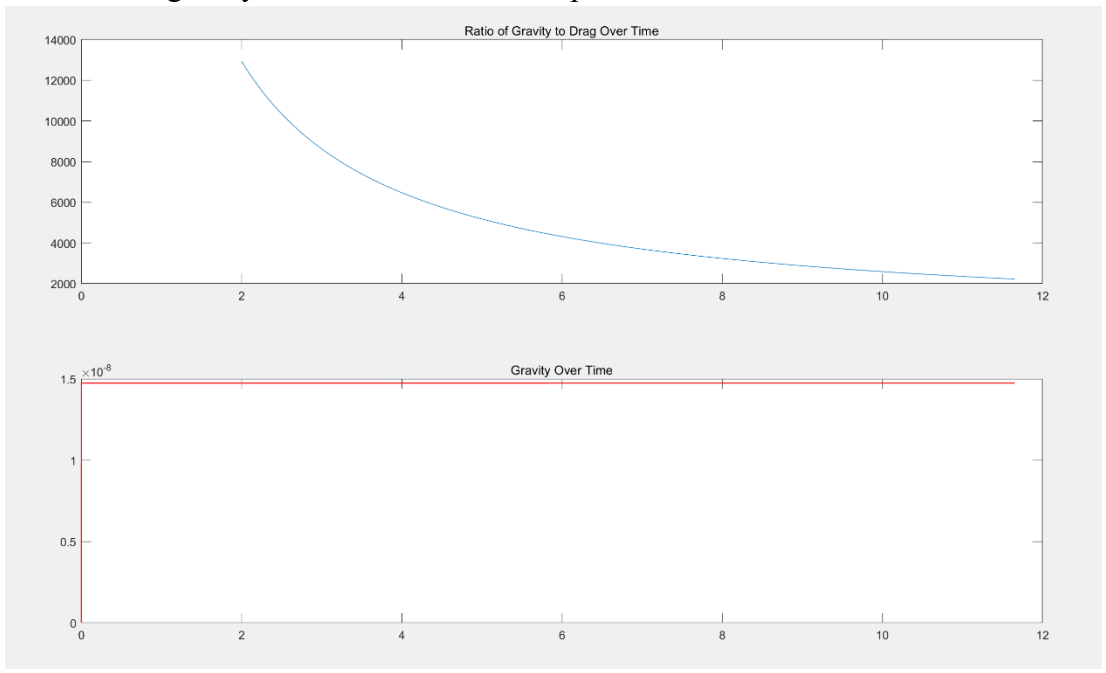


Figure 4.6 Ratio of gravity to air friction over time and value of gravity over time for air friction case.

## **4.3 Experimental Conditions**

There are two restrictions on the design of proposed experiment:

- 1. The internal acceleration of two balls should be within the MOND regime.
- 2. In order to minimize perturbations from the external environment, we limit the collision time to ten seconds.

The first constraint reads:

$$a < a_0 = 1.2 \times 10^{-10} \text{ m/s}^2$$
 (4.3.1)

From Newton's Second Law, (assuming Newtonian mechanics for order of magnitude estimation):

$$a = \frac{Gm}{(L-2x)^2} \tag{4.3.2}$$

The acceleration has to be smaller than  $a_0$  throughout collision process, which means the greatest value of a is smaller than  $a_0$ . From Equation, one can know that a increases as x increases. So,  $a(\epsilon r)$  is the maximum value.

Hence

$$\frac{Gm}{4r^2} < 1.2 \times 10^{-10} \text{ m/s}^2$$
 (4.3.3)

Substituting the value of G and writing  $m = \frac{4}{3}\pi r^3 \rho$  for a ball:

$$\rho r < 1.7 \text{kg/m}^2$$
 (4.3.4)

For platinum ball with density 2109  $kg/m^3$ , the restriction means that the radius of balls must be smaller than 0.8mm. Note that gravity from a mm-scale object has already been detected in the lab [26].

Here is the corresponding radius table for some material with densities around 100kg/m<sup>3</sup>

Material	Density (kg/m <sup>3</sup> )	Radius (cm)
Expanded Polystyrene (EPS)	20~50	3.4~8.5
Balsa Wood	160	1
Metal Foam	50~200	0.85~3.4
Silica Aerogel	100	1.7

Table 4.1: Maximum radius for balls made of various materials.

The second constraint means:

$$t = \sqrt{\frac{L}{2Gm}} \left( \sqrt{x(L - 2x)} + \frac{L\sqrt{2}\tan^{-1}(\frac{2x}{L - 2x})}{2} \right) < 10s$$
 (4.3.5)

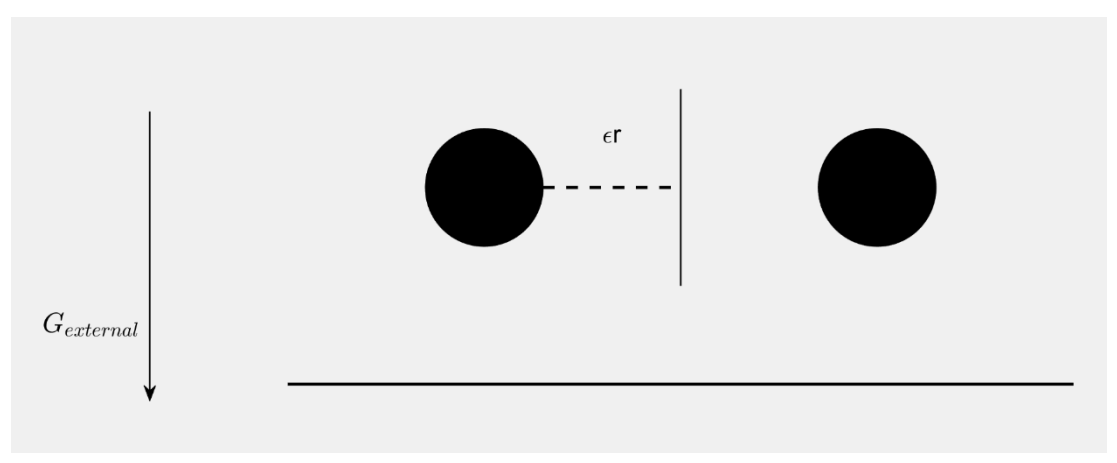


Figure 4.7 Notations used to simplify implications of 10 seconds measurement time. The black bar situated in the middle of two balls represents the position where two balls collide. The dashed line is the distance from the edge of one ball to the collision point, denoted as  $\epsilon r$ —the distance is expressed as the ball's radius multiplied by a proportionality factor.

First, we substitute  $m = \frac{4}{3}\pi r^3 \rho$  for a ball and  $L = (2 + 2\epsilon)r$  into Equation (4.3.5), see Fig. 4.7 for the notation.

Then, expand arctanx around x = 0:

$$\tan^{-1} x = x - \frac{1}{3}x^3 + \frac{1}{5}x^5 - \dots + (-1)^n \frac{x^{2n+1}}{2n+1} + \dots$$

Equation (4.3.5) becomes:

$$t = \sqrt{\frac{3+3\epsilon}{2G\pi\rho}} \left( \sqrt{\epsilon} + \epsilon + \epsilon^2 \right) \tag{4.3.6}$$

From equation (4.3.6), one can see that the collision time is independent of the radius of the ball. For a given platinum ball, its density is constant, and the collision time depends solely on  $\epsilon$ , meaning that the collision time is only related to the distance between the surfaces of two balls.

As shown in Fig. 4.8, to keep the collision time of two balls around 10 seconds,  $\epsilon$  has to be less than  $3 \times 10^{-4}$ . We already know that due to the limitation of acceleration, the radius of platinum balls must be less than 0.8 mm. So, the distance between surfaces of two platinum balls, denoted as  $2\epsilon r$ , must be less than 480 nm. This is rather demanding and means that surface effects have to be carefully considered.

Material	Density(kg/ m³)	Radius(cm)	<i>ϵ</i> (1e-7)	Distance between edges of two balls(nm)
Expanded Polystyrene (EPS)	20~50	3.4~8.5	2.8~7	23.8
Balsa Wood	160	1.0625	22.3	23.7
Metal Foam	50~200	0.85~3.4	7~28	23.8
Silica Aerogel	100	1.7	14	23.8

Table 4.2: Values of  $\epsilon$  and the associated distance between the surface of two-body system for the investigated materials.

While this study does not systematically examine the correlation between surface distance between two balls and material density, the results presented in Table 4.2 reveal that the distance shows no density dependence when the initial acceleration and collision time are fixed.

Everything discussed above regarding experimental conditions falls under the case of Newtonian mechanics. However, as we discussed in the "Air Friction" section, the motion of two balls in the air friction scenario is almost identical to the motion in the internal gravity scenario. So, all the restrictions derived above also apply to the case of air friction.

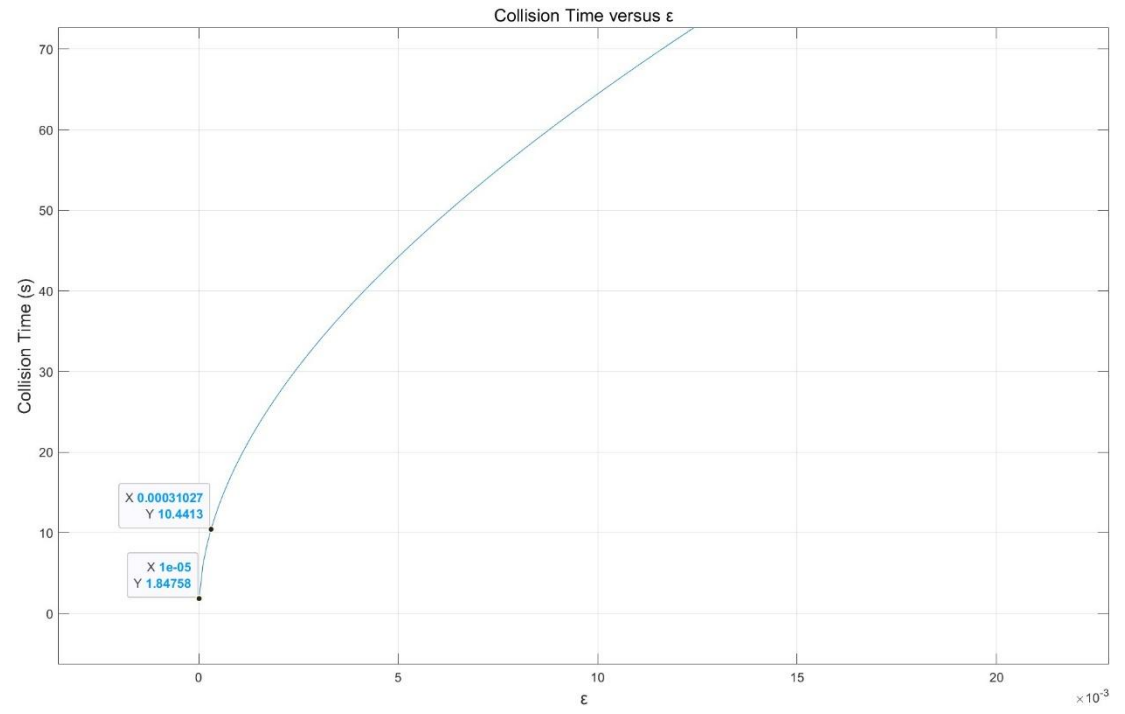


Figure 4.8 Collision time versus  $\epsilon$  for platinum ball.

# 4.4 Rotating Polar Coordinate System

The motion of two balls will be observed and recorded by a lab on Earth, which means

in a rotating reference frame.

For simplicity, we keep the motion of the two balls in two dimensions, i.e. they are placed on the equator at the beginning, and one is on top of the other (parallel configuration, see Fig. 4.1(b)).

The Lagrangian of two-ball system in 3D Cartesian coordinate system is:

$$L = \frac{1}{2}mv_1^2 + \frac{1}{2}mv_2^2 + \frac{Gm^2}{r}$$
 (4.4.1)

where r is the distance between centers of two balls. In the rotating reference frame, the Coriolis force, which is always perpendicular to the direction of motion of the object, will transform the motion of two balls from one-dimensional to two-dimensional. So, the distance between centers of two balls cannot be simply written as L - 2x.

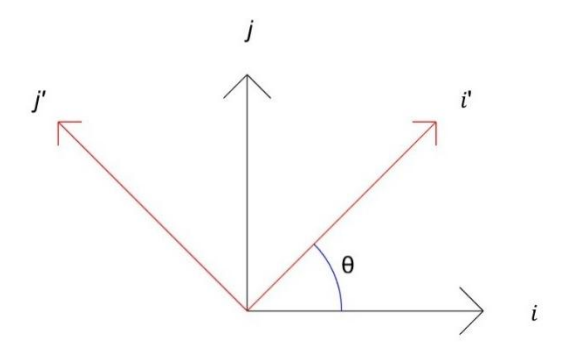


Figure 4.9 Notation used for rotating coordinate system

The velocity v and distance r in Equation (4.4.1) need to be transformed from the 3D Cartesian coordinate system into the rotating Cartesian coordinate system. The velocity of two balls in a rotating coordinate system is [26]:

$$\vec{\mathbf{v}} = (\dot{\mathbf{X}} - \dot{\mathbf{\theta}}\mathbf{Y})\hat{\mathbf{1}}' + (\dot{\mathbf{Y}} + \dot{\mathbf{\theta}}\mathbf{X})\hat{\mathbf{j}}' \tag{4.4.2}$$

where X and Y are coordinates in the rotating coordinate system, and  $\dot{\theta}$  is the angular velocity of the rotating coordinate system, see Fig. 4.9. In our experiment, it is the angular velocity of earth rotation, denoted as  $\omega$ . Equation (4.4.2) gives the velocity of an object as observed from the rotating coordinate system, which rotates around its own origin. However, in a real-life scenario, the object actually rotates around the center of the Earth. Therefore, the rotation of the origin should be incorporated into Equation (4.4.2).

This results in the modified Equation (4.4.2):

$$\vec{\mathbf{v}} = (\dot{\mathbf{X}} - \dot{\mathbf{\theta}}\mathbf{Y} - a)\hat{\mathbf{i}}' + (\dot{\mathbf{Y}} + \dot{\mathbf{\theta}}\mathbf{X})\hat{\mathbf{j}}' \tag{4.4.3}$$

Letter a represents the contribution of the rotation of the origin. The angular velocity is considered constant because the collision time between the two balls is expected to be around 10 seconds. The Earth's rotation period is one day which is 86,400 seconds. Ten seconds is a relatively small-time interval when compared to that number, meaning the angle by which the Earth rotates in 10 seconds is negligible. Thus, the change in the direction of the translational velocity of the rotating origin is negligible. Over 10 seconds, the change in the angular velocity of Earth's rotation is also negligible. Therefore, the translational velocity of the rotating origin,  $v_t = \omega r$ , can be treated as a constant in our discussion, which is denoted by a, where r is the distance between the observer and the center of the Earth.

The distance between center of two balls as interpreted in rotating coordinate system is simply written as:

$$r = \sqrt{(X_1 - X_2)^2 + (Y_1 - Y_2)^2}$$
 (4.4.4)

where  $X_1$  and  $Y_1$  are the coordinates of one ball in the rotating coordinate system,  $X_2$  and  $Y_2$  are the coordinate of another ball in the rotating coordinate system.

Substituting Equation (4.4.4) and Equation (4.4.3) into Equation (4.4.1):

$$\begin{split} L &= \ \frac{1}{2} m \big( \dot{X}_1^2 + \dot{Y}_1^2 \big) + \frac{1}{2} m \omega^2 (X_1^2 + Y_1^2) + m \omega \big( \dot{Y}_1 X_1 - \dot{X}_1 Y_1 \big) - m a \dot{X}_1 + m a \omega Y_1 \\ &+ 2 a^2 + \frac{1}{2} m \big( \dot{X}_2^2 + \dot{Y}_2^2 \big) + \frac{1}{2} m \omega^2 (X_2^2 + Y_2^2) + m \omega \big( \dot{Y}_2 X_2 - \dot{X}_2 Y_2 \big) - m a \dot{X}_2 + m a \omega Y_2 \\ &+ \frac{G m^2}{\sqrt{(X_1 - X_2)^2 + (Y_1 - Y_2)^2}} \end{split}$$

Then transform the coordinates from Cartesian coordinates into polar coordinates:

$$\begin{cases} X_1 = r_1 \cos \phi_1, & Y_1 = r_1 \sin \phi_1 \\ X_2 = r_2 \cos \phi_2, & Y_2 = r_2 \sin \phi_2 \end{cases}$$

Where  $r_1$  and  $\varphi_1$  are the coordinates of one ball in polar coordinate system,  $r_2$  and  $\varphi_2$  are the coordinates of another ball in polar coordinate system.

Hence the Lagrangian for two balls system in rotating polar coordinate system is:

$$\begin{split} L &= \frac{1}{2} m (\dot{r}_1^2 + r_1^2 \dot{\phi}_1^2) + \frac{1}{2} m \omega^2 r_1^2 + m \omega r_1^2 \dot{\phi}_1 + m \alpha r_1 (\omega - \dot{\phi}_1) \sin \phi_1 \\ &- m \alpha \dot{r}_1 \cos \phi_1 + \frac{1}{2} m (\dot{r}_2^2 + r_2^2 \dot{\phi}_2^2) + \frac{1}{2} m \omega^2 r_2^2 + m \omega r_2^2 \dot{\phi}_2 + m \alpha r_2 (\omega - \dot{\phi}_2) \sin \phi_2 \\ &- m \alpha \dot{r}_2 \cos \phi_2 + \frac{G m^2}{\sqrt{r_1^2 + r_2^2 - 2 r_1 r_2 \cos(\phi_1 - \phi_2)}} \end{split}$$

By writing  $\frac{d}{dt} \frac{\partial L}{\partial \dot{r}_1} = \frac{\partial L}{\partial r_1}$ ,  $\frac{d}{dt} \frac{\partial L}{\partial \dot{r}_2} = \frac{\partial L}{\partial r_2}$ ,  $\frac{d}{dt} \frac{\partial L}{\partial \dot{\varphi}_1} = \frac{\partial L}{\partial \varphi_1}$ ,  $\frac{d}{dt} \frac{\partial L}{\partial \dot{\varphi}_2} = \frac{\partial L}{\partial \varphi_2}$ , we shall get the equation of motion for two balls in rotating polar coordinate system. But there are eight variables in the above four equations, which is  $\dot{r}_1 \ \dot{r}_2 \ \dot{\varphi}_1 \ \dot{\varphi}_2$  and  $\ddot{r}_1 \ \ddot{r}_2 \ \ddot{\varphi}_1 \ \ddot{\varphi}_2$ . So there is no analytical solution, but the system can be simulated numerically.

#### 4.5 Rough Trajectory and Collision Time

When observing the motion of an object in a rotating reference frame, a fictitious force called the Coriolis force is introduced [26]:

$$F_c = -2m\boldsymbol{\omega} \times \boldsymbol{v} \tag{4.5.1}$$

where  $\omega$  is the angular velocity of the rotating frame, v is the velocity of the object. The Coriolis force is always perpendicular to the velocity of the object, hence causing its trajectory to curve.

Because the gravitational attraction between the two small spheres is mutual,

$$F = G \frac{Mm}{(L-2x)^2} \tag{4.5.2}$$

The values of the accelerations and velocities of the two balls are the same. Hence, the two balls will collide at the midpoint of the initial positions of the two balls.

Therefore, an observer in the rotating reference frame would see the two balls orbiting around their midpoint while gradually approaching each other—spiral motion, see Fig. 4.10.

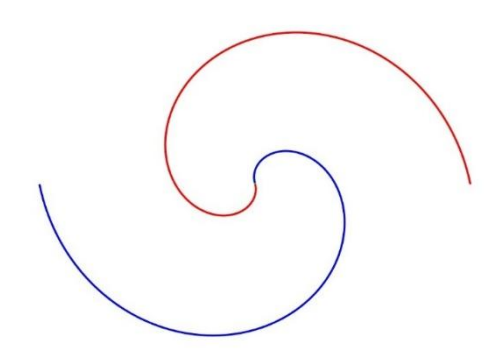


Figure 4.10 Schematic diagram of spiral motion

The ratio of radial velocity to angular velocity is an important parameter in spiral motion. It describes how curved the trajectory is. For simplicity, we plot the trajectories of spiral motions with constant radial, angular velocities and different ratio parameter k.

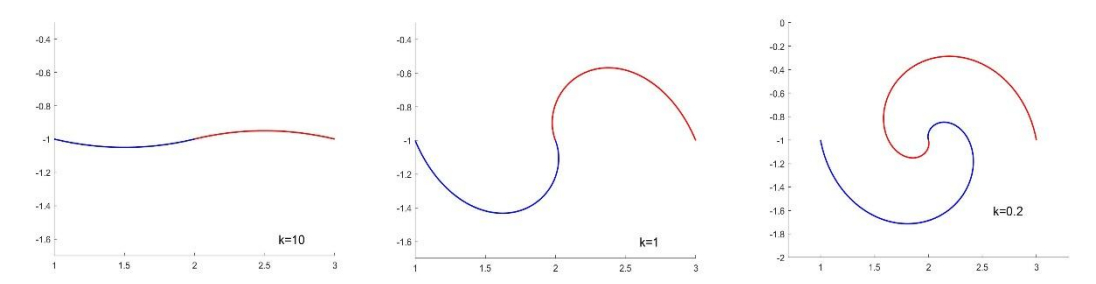


Figure 4.11 Trajectories of spiral motions with different ratios. We can see in Fig. 4.11 that the ratio of radial velocity to angular velocity is crucial. In our proposed setup, the initial radial and angular velocities of the two balls are zero. So,  $k = v_{radial}/\omega = \frac{a_{radial}}{a_{angular}} = Gravity/Coriolis force$ . We need to find out the ratio of internal gravity to Coriolis force, see Fig 4.12.

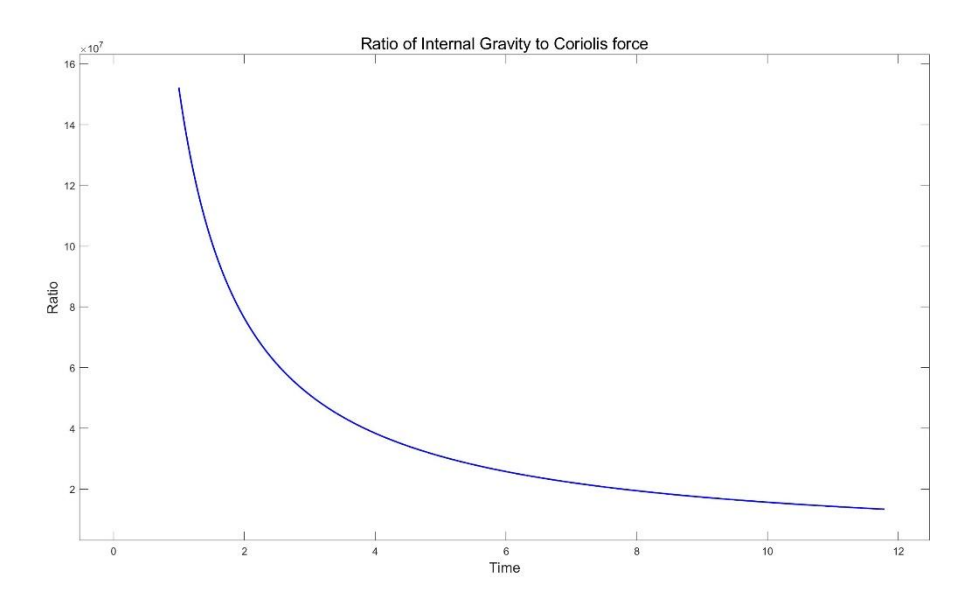


Figure 4.12 Ratio of internal gravity to Coriolis force Reading from Fig 4.12, we know that the ratio is always greater  $1 \times 10^7$ , we can then plot the trajectory of spiral motion with  $k = 1 \times 10^7$ , see figure below.

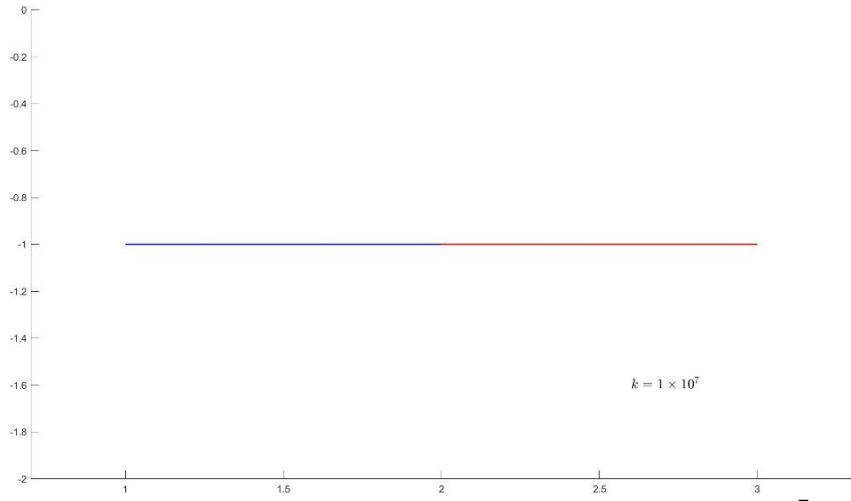


Figure 4.13 Trajectory of spiral motion with  $k = 1 \times 10^7$ 

The ratio of internal gravity to Coriolis force is extremely high—the effect of Coriolis force is negligible. It can also be found in Fig. 4.13 that the trajectory is visually flat. Therefore, although we observe the motion of the two small balls in a rotating reference frame, i.e. Earth, their trajectories should still be such that they collide directly with each other without any rotation around the midpoint.

Since we introduced EFE, the quantity we are interested in is the collision time, especially the difference of collision time between two different setups, see Fig. 4.1. For the setup that the axis joining centers of two balls is orthogonal to the external field, two balls will experience mutual gravitational attraction toward each other and external field that pulls the whole two-body system downward. In the setup that the axis joining centers of two balls parallels the external field, the small ball at the lower position will experience an upward mutual gravitational attraction and a downward external gravitational force, while the small ball at the upper position will experience a downward mutual attractive force and a downward external gravitational force—the EFE needs to be taken into account. Hence the dynamics of the two-body system is different in two setups.

The collision time has already been given in section 4.3 equation (4.3.5) and (4.3.6):

$$t = \sqrt{\frac{L}{2Gm}} \left( \sqrt{x(L - 2x)} + \frac{L\sqrt{2}\tan^{-1}\left(\frac{2x}{L - 2x}\right)}{2} \right)$$
$$t = \sqrt{\frac{3 + 3\epsilon}{2G\pi\rho}} \left( \sqrt{\epsilon} + \epsilon + \epsilon^2 \right)$$

Since the EFE can be quantified as the modification to the gravitational constant G. To calculate the collision time in parallel setup, we need to substitute a modified gravitational constant  $G_{eff}$ :

$$t_{eff} = \sqrt{\frac{3+3\epsilon}{2G_{eff}\pi\rho}} \left(\sqrt{\epsilon} + \epsilon + \epsilon^2\right) = \left(\sqrt{\mu_e\sqrt{1+\lambda_e sin^2\theta}}\right) t$$

Hence

$$\Delta t = \left(1 - \sqrt{\mu_e \sqrt{1 + \lambda_e sin^2 \theta}}\right) t$$

where  $\theta=\pi/2$ ,  $g_e=9.8\,m/s^2$ ,  $\mu_e=\mu(y_e)$ ,  $\lambda_e=y_e\,\mu_e'/\mu_e$ ,  $\mu_e'=d\mu(y_e)/dy_e$  and  $y_e=g_e/a_0$ . Let the interpolating function be the simple  $\mu$  function:  $\mu(x)=x/1+x$ .

Assume the collision time t = 10s. Then

$$\Delta t = 3.061106923496482 \times 10^{-12} \times 10s = 3.061106923496482 \times 10^{-11}s$$

The collision time difference between two setups is 30ps. In our setup, although the external field is Earth's gravitational field g, which is much larger than  $a_0$ , we still expect an external field effect to emerge, even if this effect is extremely weak.

To observe this tiny difference is too challenging. To increase the time difference, we need to either increase to collision time or use a weaker external field such that the value of  $\sqrt{\mu_e\sqrt{1+\lambda_e sin^2\theta}}$  is smaller.

## **CHAPTER 5**

### **CONCLUSION**

This work tries to find ways to experimentally verify the External Field Effect (EFE) that Modified Newtonian Dynamics (MOND) introduces, MOND is an alternative model, explaining some dark matter phenomenology. With a streamlined two-body approach, the study determines the necessary physical and theoretical conditions needed to observe EFE in a lab. Using analysis and computer simulations, including Runge-Kutta method, the system of two identical masses moving under each other's gravitational pull was studied. The findings give numerical estimates of the predicted motion and list the conditions needed to stay in the MOND regime.

Two major constraints emerged from the analysis: the internal acceleration must remain below the MOND critical acceleration scale, and the experimental timescale should be small to avoid environmental disturbance. These restrictions translate into strict requirements on material density, object size, and initial separation. For example, platinum spheres must have radii less than 0.8 mm, and edge separations must be on the order of hundreds of nanometers, to ensure that the system remains in the MOND regime for the duration of the collision process.

Future work may expand on this foundation by refining the experimental setup. Enhancing time resolution through high-precision sensors are essential next steps. Simulations of exact trajectories of the two-body system under horizontal and vertical alignment is also important.

#### REFERENCES

- [1] Zwicky, F. (1933). Die Rotverschiebung von extragalaktischen Nebeln. *Helvetica Physica Acta*, 6, 110–127.
- [2] Rubin, V. C. (1983). The rotation of spiral galaxies. *Science*, 220(4604), 1339–1344.
- [3] Ade, P. a. R., Aghanim, N., Armitage-Caplan, C., Arnaud, M., Ashdown, M., Atrio-Barandela, F., . . . Hobson, M. (2014). Planck2013 results. XVI. Cosmological parameters. *Astronomy and Astrophysics*, *571*, A16.
- [4] Bernabei, R., Belli, P., Cappella, F., Montecchia, F., Nozzoli, F., Incicchitti, A., . . . Ye, Z. (2003). Results from DAMA/NaI and perspectives for DAMA/LIBRA. *arXiv* (Cornell University).
- [5] Akerib, D. S., Araújo, H. M., Bai, X., Bailey, A. J., Balajthy, J., Bedikian, S., . . . Zhang, C. (2014). First Results from the LUX Dark Matter Experiment at the Sanford Underground Research Facility. *Physical Review Letters*, 112(9).
- [6] Aprile, E., Aalbers, J., Agostini, F., Alfonsi, M., Althueser, L., Amaro, F. D., . . . Mougeot, X. (2020). Excess electronic recoil events in XENON1T. *Physical Review. D/Physical Review. D.*, 102(7).
- [7] Milgrom, M. (1983). A modification of the Newtonian dynamics as a possible alternative to the hidden mass hypothesis. *The Astrophysical Journal*, 270, 365.
- [8] Corbelli, E., & Salucci, P. (2000). The extended rotation curve and the dark matter halo of M33. *Monthly Notices of the Royal Astronomical Society, 311*(2), 441–447.
- [9] De Leo M. (2018). Rotation curve of spiral galaxy Messier 33. Retrieved from https://en.wikipedia.org/wiki/Galaxy rotation curve
- [10] Clowe, D., Bradač, M., Gonzalez, A. H., Markevitch, M., Randall, S. W., Jones, C., & Zaritsky, D. (2006). A direct empirical proof of the existence of dark matter. *The Astrophysical Journal*, 648(2), L109–L113.
- [11] Famaey, B., & McGaugh, S. S. (2012). Modified Newtonian Dynamics (MOND): Observational Phenomenology and Relativistic Extensions. *Living Reviews in Relativity, 15*(1).
- [12] Milgrom, M. (1994). Dynamics with a Nonstandard Inertia-Acceleration Relation: An Alternative to Dark Matter in Galactic Systems. *Annals of Physics*, 229(2), 384–415.

- [13] Milgrom, M. (1994b). Modified dynamics predictions agree with observations of the H I kinematics in faint dwarf galaxies contrary to the conclusions of Lo, Sargent, and Young. *The Astrophysical Journal*, 429, 540.
- [14] Bekenstein, J., & Milgrom, M. (1984). Does the missing mass problem signal the breakdown of Newtonian gravity? *The Astrophysical Journal*, 286, 7.
- [15] Clifton, T., Ferreira, P. G., Padilla, A., & Skordis, C. (2012). Modified gravity and cosmology. *Physics Reports*, 513(1–3), 1–189.
- [16] Milgrom, M., & Sanders, R. H. (2008). Rings and shells of "Dark Matter" as MOND artifacts. *The Astrophysical Journal*, 678(1), 131–143.
- [17] Gentile, G., Famaey, B., & De Blok, W. J. G. (2010). THINGS about MOND. *Astronomy and Astrophysics*, 527, A76.
- [18] Magueijo, J., & Bekenstein, J. (2007). TESTING STRONG MOND BEHAVIOR IN THE SOLAR SYSTEM. *International Journal of Modern Physics D*, 16(12a), 2035–2053.
- [19] Lelli, F., McGaugh, S. S., & Schombert, J. M. (2016). SPARC: MASS MODELS FOR 175 DISK GALAXIES WITH SPITZER PHOTOMETRY AND ACCURATE ROTATION CURVES. *The Astronomical Journal*, *152*(6), 157.
- [20] Begeman, K. G., Broeils, A. H., & Sanders, R. H. (1991). Extended rotation curves of spiral galaxies: dark haloes and modified dynamics. *Monthly Notices of the Royal Astronomical Society*, 249(3), 523–537.
- [21] Tully, R., & Fisher, J. (1977). A New method of determining distances to galaxies. *Astronomy and Astrophysics*, *54*, 661–673.
- [22] De Blok, W. J. G., Walter, F., Brinks, E., Trachternach, C., Oh, S., & Kennicutt, R. C. (2008). HIGH-RESOLUTION ROTATION CURVES AND GALAXY MASS MODELS FROM THINGS. *The Astronomical Journal*, *136*(6), 2648–2719.
- [23] Bell, E. F., McIntosh, D. H., Katz, N., & Weinberg, M. D. (2003). The Optical and Near-Infrared Properties of galaxies. I. Luminosity and stellar mass functions. *The Astrophysical Journal Supplement Series*, 149(2), 289–312.
- [24] McGaugh, S. S. (2005). The Baryonic Tully-Fisher Relation of Galaxies with Extended Rotation Curves and the Stellar Mass of Rotating Galaxies. *The Astrophysical Journal*, 632(2), 859–871.
- [25] Laidler, K. J. (1994). The world of physical chemistry. Choice Reviews Online,

*31*(09), 31–4921.

[26] Coriolis force in rotating reference frames. (2022, January 26). *University Polytechnic of Madrid*. Retrieved from

https://blogs.upm.es/ddcampayo/wpcontent/uploads/sites/279/2022/01/Coriolis.pdf

#### **APPENDIX**

Code for Figure 3.4 Velocity and Position over time for both internal gravity and air friction cases

```
clc: clear:
% 参数设置
G = 6.67430e-11; % 引力常数 (m<sup>3</sup> kg<sup>-1</sup> s<sup>-2</sup>)
r = 0.01:
                 % 小球半径 (m)
epsi = 1e-4;
dp = 2.109e4:
                 % 铂密度 = 2.109e4 (kg/m<sup>3</sup>)
m = (4/3)*pi*(r<sup>3</sup>)*dp; % 小球质量 (kg)
L = (2 + 2*epsi)*r; % 两球间初始距离 (m)
eta = 1.81e-5; % 空气粘度 (Pa.s)
% 初始条件
x0 = 0;
                % 初始位置 (m)
                 % 初始速度 (m/s)
v0 = 0;
% 时间设置
t0 = 0;
                 % 初始时间(s)
t end = 1000;
                % 结束时间 (s)
h = 0.001;
                 % 时间步长(s)
N = floor((t_end - t0) / h); % 步数
% 初始化
t = t0:
Y drag = [x0; v0]; % 状态向量 [x; v]
Y no drag = [x0; v0]; % 状态向量 [x; v]
% 用于记录结果
results drag = zeros(N+1, 3); % 考虑空气阻力的结果
results_no_drag = zeros(N+1, 3);% 不考虑空气阻力的结果
results drag(1, :) = [t, x0, v0];
results_no_drag(1, :) = [t, x0, v0];
% 四阶 Runge-Kutta 法实现(考虑空气阻力和不考虑空气阻力的两种情况)
for n = 1:N
   kl drag = h * derivatives(t, Y drag, L, r, m, eta, true); % 考虑空气阻力
   k2_drag = h * derivatives(t + h/2, Y_drag + k1_drag/2, L, r, m, eta, true);
   k3_drag = h * derivatives(t + h/2, Y_drag + k2_drag/2, L, r, m, eta, true);
   k4_drag = h * derivatives(t + h, Y_drag + k3_drag, L, r, m, eta, true);
```

kl\_no\_drag = h \* derivatives(t, Y\_no\_drag, L, r, m, eta, false); % 不考虑空气阻力

```
k2\_no\_drag = h * derivatives(t + h/2, Y\_no\_drag + k1\_no\_drag/2, L, r, m,
eta, false);
   k3_{no}drag = h * derivatives(t + h/2, Y_{no}drag + k2_{no}drag/2, L, r, m,
eta, false);
   k4_{no\_drag} = h * derivatives(t + h, Y_{no\_drag} + k3_{no\_drag}, L, r, m, eta,
false);
   % 更新状态向量
   Y drag = Y drag + (1/6) * (k1 drag + 2*k2 drag + 2*k3 drag + k4 drag); %
考虑空气阻力
   Y_no_drag = Y_no_drag + (1/6) * (k1_no_drag + 2*k2_no_drag + 2*k3_no_drag
+ k4_no_drag); % 不考虑空气阻力
   t = t + h; % 更新时间
   % 记录结果
   results_drag(n + 1, :) = [t, Y_drag(1), Y_drag(2)];
   results_no_drag(n + 1, :) = [t, Y_no_drag(1), Y_no_drag(2)];
   % 检查位置,如果 x 大于 L/2,停止计算
   if abs(Y drag(1)) > L/2 - r
       results_drag = results_drag(1:n+1, :); % 保留有效结果
       results no drag = results no drag(1:n+1, :); % 保留有效结果
       break; % 退出循环
   end
end
% 绘图
figure;
subplot (2, 1, 1);
plot(results drag(:, 1), results drag(:, 2), 'b-', 'LineWidth', 1.5); % 计算
考虑空气阻力的情况,蓝色线
hold on:
plot(results_no_drag(:, 1), results_no_drag(:, 2), 'r--', 'LineWidth', 1.5); %
计算不考虑空气阻力的情况, 红色线
xlabel('Time (s)', 'FontSize', 14);
ylabel('Displacement (m)', 'FontSize', 14);
title ('Displacement of the Ball Over Time', 'FontSize', 14);
legend({'With Air Drag', 'Without Air Drag'}, 'FontSize', 12);
grid on;
subplot (2, 1, 2);
plot(results_drag(:, 1), results_drag(:, 3), 'b-', 'LineWidth', 1.5); % 速度
```

图,考虑空气阻力的情况,蓝色线

```
hold on;
plot(results_no_drag(:, 1), results_no_drag(:, 3), 'r--', 'LineWidth', 1.5); %
速度图,不考虑空气阻力的情况,红色线
xlabel('Time (s)', 'FontSize', 14);
ylabel('Velocity (m/s)', 'FontSize', 14);
title ('Velocity of the Ball Over Time', 'FontSize', 14);
legend({'With Air Drag', 'Without Air Drag'}, 'FontSize', 12);
grid on;
% 导数函数
function dYdt = derivatives(t, Y, L, r, m, eta, include_drag)
   G = 6.67430e-11; % 引力常数 (m<sup>3</sup> kg<sup>-1</sup> s<sup>-2</sup>)
   X = Y(1);
                     % 位置
   v = Y(2);
                  % 速度
   % 计算引力
   gravity = G * m / (L - 2*x)^2;
   % 根据是否考虑空气阻力, 计算加速度
   if include drag
       drag = 6 * pi * eta * r * v / m;
       dvdt = gravity - drag; % 空气阻力影响
   else
       dvdt = gravity; % 不考虑空气阻力
   end
   dYdt = [v; dvdt]; % 返回速度和加速度
   % 调试输出
   % disp(['Gravity: ', num2str(gravity), ', Drag: ', num2str(drag)]);
\quad \text{end} \quad
```